

Radiation Pressure Effects in a Suspended Fabry-Perot Cavity

by

Jason Scott Pelc

Submitted to the Department of Physics
in partial fulfillment of the requirements for the degree of

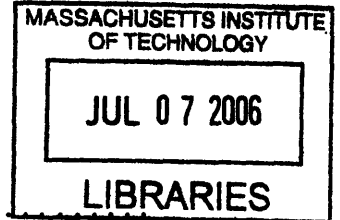
Bachelor of Science in Physics

at the

MASSACHUSETTS INSTITUTE OF TECHNOLOGY

June 2006

© Massachusetts Institute of Technology 2006. All rights reserved.

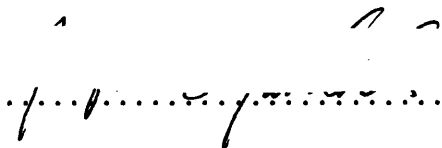


Author 

Department of Physics

May 12, 2006

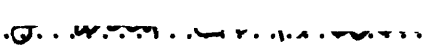
ARCHIVES

Certified by 

Nergis Mavalvala

Cecil & Ida Green Career Development Professor

Thesis Supervisor

Accepted by 

David E. Pritchard

Senior Thesis Coordinator, Department of Physics

Radiation Pressure Effects in a Suspended Fabry-Perot Cavity

by

Jason Scott Pelc

Submitted to the Department of Physics
on May 12, 2006, in partial fulfillment of the
requirements for the degree of
Bachelor of Science in Physics

Abstract

We report on experimental observation of radiation-pressure induced effects in a high-power optical cavity. These effects play an important role in next generation gravitational wave detectors, as well as quantum non-demolition devices. We describe two experiments in which a low-transmission input mirror and near-perfectly-reflective end mirror are suspended as pendulums.

A unified model of optomechanical coupling is presented, whereby a strong coherent laser field interacts with a classical harmonic oscillator. We show that such a system is well described using standard techniques from control theory.

We measure the properties of an optical spring, whereby the optical field increases the rigidity of the pendulum mode of the mirrors; during our first (Phase 1) experiment, we measure an optical rigidity of $K_0 = (3.08 \pm 0.09) \times 10^4$ N/m, corresponding to an optical rigidity that is 6000 times stiffer than the mechanical stiffness. In our second (Phase 2) experiment with higher finesse and lower mirror mass, we find an unprecedented optical rigidity $K_0 = (9.60 \pm 0.12) \times 10^5$ N/m. We also measure and characterize the parametric instability, caused by the coupling of the cavity field to the acoustic modes of the mirror, and find an instability strength $R \approx 3$.

We discuss the noise suppression features of an optically rigid system, and demonstrate a strong-coupling radiation pressure cooling of the mirror motion. A discussion of the path towards a measurement of the quantum mechanical state of the bulk mirror motion in future experiments is included.

Thesis Supervisor: Nergis Mavalvala

Title: Cecil & Ida Green Career Development Professor

Acknowledgments

Firstly, I'd like to thank my supervisor Nergis Mavalvala, who not only got me interested in this fascinating field, but subsequently provided clear physical insight, much helpful guidance, and beer on several Friday afternoons.

I am supremely indebted to Thomas Corbitt, with whom I have worked most closely for the past year. Thomas was always there to explain the details, and his late night (or extremely early morning) diligence produced much of the data presented in this work. Thomas also created the “unified model” of optical rigidity described here, and conceived the design for the composite mirror suspension used during Phase 2.

Lastly, I'd like to thank my parents, for first getting me interested in Science, and subsequently sending MIT lots of money over the last four years to make my life very difficult.

Contents

1	Introduction	13
1.1	Summary of Previous Work	14
1.2	Outline	16
2	Theory of Radiation Pressure Effects	19
2.1	Fabry-Perot basics	19
2.2	Radiation Pressure forces	23
2.3	Unified Model of Optical Rigidity	24
2.3.1	Quasistatic Motion	25
2.3.2	Frequency Domain Feedback Description	27
2.4	Optical Spring Effect and Noise Suppression	29
2.5	Parametric Instability	32
3	Apparatus and Control Systems	35
3.1	Experimental Setup	35
3.1.1	Damping Control	36
3.1.2	Interferometric Sensing and Control	37
3.2	Mirrors and Suspensions	42
3.2.1	Phase 1: Large Optics	42
3.2.2	Phase 2: Composite EM	42
3.3	Physics and Control System Simulation	43
4	Results and Conclusions	47

4.1	Parametric Instability	47
4.1.1	Variation with Cavity Detuning	48
4.1.2	Determination of the Modal Mass	51
4.1.3	Variation with Input Power	52
4.2	P1 Optical Spring	52
4.3	P2 Optical Spring	55
4.3.1	Loop Gain Measurement	56
4.3.2	Optical Spring Characterization	57
4.3.3	Noise Suppression	59
4.4	Towards the Quantum Limit	59
4.5	Concluding Remarks	61

List of Figures

2-1	Optical fields and mirror parameters for the Fabry-Perot cavity. . . .	20
2-2	Analytical and Lorentzian approximations to the cavity power storage $W(I_0, \delta_\gamma)$ for a cavity with IM power transmission of 0.3 and EM reflectivity of 1.	22
2-3	Illustration of differing optomechanical dynamics depending on the sign of the detuning δ_γ . In (a), positive δ_γ gives a restoring force, whereas in (b) the negative δ_γ gives an anti-restoring force.	27
2-4	Representation of the optical rigidity as a feedback system.	28
2-5	Numerical calculation of $P_{OR}(\Omega)$ based on Eq. (2.27) for Phase 2 cavity parameters and three values of K_0	31
3-1	Schematic representation of the experiment. Approximately 5 W of intensity- and frequency-stabilized 1064 nm Nd:YAG laser light is incident on a Fabry Perot cavity. EOM refers to electrooptic modulator; MX to mixer; PD to photodetector; and QWP to quarter-wave plate.	37
3-2	Electronic length and frequency control transfer functions $H_L(\Omega)$ and $H_f(\Omega)$. The overall scaling is adjustable, and the frequency dependence of the sensing and length actuation mechanisms is not accounted for.	39
3-3	Plots of $L(\Omega)$ and $F(\Omega)$ for typical gains G_L and G_f , yielding crossover frequency $\Omega_c \approx 300$ Hz and locking bandwidth $\Omega_b \approx 4$ kHz.	41
3-4	(a) Illustration of composite mirror and (b) fiber flexing effect due to thermal expansion.	43
3-5	Block diagram for the optomechanical and control systems.	44

4-1	Zoom view of PI ringup data for $R > 1$. The \times 's are measured data points, and the dashed curve is a 5 parameter fit to Eq. (4.5).	50
4-2	The PI Susceptibility is plotted against the normalized detuning δ_γ for constant input power. The solid curve is a theoretical prediction with no free parameters.	51
4-3	The PI Susceptibility is plotted against the input power for constant detuning. The solid curve is a two parameter fit, allowing for uncertainty in the scaling of the power and	53
4-4	P1 OS transfer function $P_{OR}(\Omega)$ data (dots) and 1 parameter fit of Θ (solid), found to be $2\pi \times (79 \pm 1)$ Hz.	54
4-5	Coherence of $G_{loop}(\Omega)$ measurement for the $\Theta \approx 2.5$ kHz OS measurement. The coherence is unity except at the longitudinal resonance near 170 Hz and the pitch resonance near 350 Hz.	56
4-6	OS transfer functions $P_{OR}(\Omega)$ calculated from loop gain data and fit parameters according to Eq. (4.10) for four values of Θ between $2\pi \times 550$ Hz and $2\pi \times 5$ kHz. The solid black curve is the unmodified end mirror response $P_E(\Omega)$, and along with each dataset is its corresponding fit.	63
4-7	Plot of normalized residual $E(\Omega)$, defined in Eq. (4.11), for the 5 kHz OS.	64
4-8	Illustration of noise suppression: ratio of optically stiffened pendulum response to EM response at $\Omega = 2\pi \times 100$ Hz as a function of Θ	64

List of Tables

3.1 P1 and P2 cavity parameters, symbols, and values.	36
---	----

Chapter 1

Introduction

As early as 1935, Erwin Schrödinger realized that there was nothing in the developing quantum theory of matter that forbade a macroscopic object from being in a superposition of states [1]. For example, the infamous “Schrödinger Cat” state consists of all N particles in a system being simultaneously in two states:

$$|\text{cat}\rangle = \frac{1}{\sqrt{2}} (|000\dots 00\rangle + |111\dots 11\rangle). \quad (1.1)$$

Quantum interference effects from such states when N exceeds 6 are spectacularly difficult to observe, due to decoherence induced by the surrounding environment [2]. Nevertheless, in recent years there has been a serious effort put forth by theoreticians and experimentalists alike to devise situations in which one might hope to measure quantum mechanical properties of macroscopic objects. Some proposals feature tiny (nm to μm size) mechanical devices [3, 4, 5], while others attempt to construct superposition states of superconducting devices [6] or large organic molecules [7]. These diverse systems share one unifying feature: they use the term “macroscopic” fairly loosely. None would be visible to the naked eye.

One realistic proposal exists whereby it may be possible to cool a 1 g mirror to a level in which its quantum mechanical effects might become apparent [8]. The work in this thesis describes the classical physics that is used to provide such a tremendous “cooling”, the coupling of a harmonic oscillator to an intense optical field. Much of

the work is described in a manuscript recently submitted by our group to Physical Review Letters [9], and excerpts from it appear (at times verbatim) in this thesis.

1.1 Summary of Previous Work

The effects we describe are due to radiation pressure, which is typically a famously weak effect. Recall, for example, that one would need a square kilometer of mirrors at the earth's distance from the sun just to generate 9 N of thrust by radiation pressure. The use of high-Finesse Fabry-Perot cavities allows the storage of tremendous amounts of power such that radiation pressure effects move out of the background and become the dominant physical effect.

For optomechanical coupling to occur in Fabry-Perot cavities via radiation pressure, some mechanism must linearly couple the phase fluctuations induced by mechanical motion to intensity fluctuations of the intracavity field. One such mechanism is to detune the laser frequency from the center of the cavity resonance, such that the stored power (and hence the radiation pressure force) has a linear dependence on the cavity length. Depending on which side of the resonance the cavity is detuned, the force can either be restoring, dubbed the Optical Spring (OS), or anti-restoring.

The OS effect occurs when the optical restoring force on the cavity mirrors is comparable to, or greater than, the mechanical restoring force, and the resonant frequency of the optomechanical system is shifted. A previous demonstration of the OS effect [10] showed a 2% shift in the resonant frequency corresponding to an optical rigidity that was 25 times weaker than the mechanical rigidity. An important feature of the OS, which was not accessible to previous experiments due to the relative weakness of the OS, is that there is also a radiation pressure force proportional to the velocity of the cavity mirrors, which arises from the time delay in the cavity response. When the cavity detuning is redshifted to create an OS, this time delay leads to a force in the same direction as the instantaneous mirror velocity, and the optical field pumps energy into the kinetic energy of the mirrors. If the mechanical viscous damping of the mirrors is not sufficient to remove this energy, then the OS will become

unstable [11, 12]. Another important feature of the OS is that at frequencies below the optomechanical resonance, the response of the system to external disturbances (e.g., driven by seismic or thermal forces) is suppressed by the optical rigidity. This effect makes the optical spring an important feature in QND interferometers [8], whose performance may otherwise be limited by thermal forces. In this work, we report on an experiment that demonstrates an optical rigidity that is 6000 times stiffer than the mechanical rigidity. In the strong coupling regime of our experiment, the unstable nature of the optical spring is exposed for the first time, and we show how it may be controlled.

For cases in which the optical rigidity is much weaker than the mechanical rigidity, it would seem that optomechanical effects should be negligible. However, though the optomechanical resonant frequency will be only slightly shifted from the mechanical resonant frequency, the viscous optical force may still have a strong effect, if it is of the same order as the mechanical viscous damping. The behavior of the system at resonance is dominated by the damping, and may show parametric instability (PI) if the optical damping is stronger than the mechanical damping. The optical damping may either viscously damp (blueshifted, cold damping) or excite (redshifted, PI) the motion. This effect is predominately important for the acoustic modes of mirrors, which are extremely stiff and have extremely small mechanical damping. Kippenberg et al. observed PIs in ultrahigh-Q toroidal optical microcavities, at frequencies of 4.4 to 49.8 MHz and modal masses of 10^{-8} to 10^{-9} kg [13]. Enhancement or reduction of the damping of a microlever at a similar mass scale has also been demonstrated [14]. PIs are also predicted to occur in advanced gravitational-wave detectors [15, 16, 17, 18], although the optomechanical coupling mechanism is different. In these detectors, the linewidths of the cavities are on the order of 100 Hz, while the acoustic mirror modes have frequencies of 10 kHz, well outside the linewidth of the cavities. For PI to occur in this regime, it is necessary to excite higher order eigenmodes of the optical beam which overlap both spectrally and spatially with the mirror acoustic mode. Additionally, the lower and upper (Stokes and anti-Stokes) optical modes must have different optical gains to provide phase to intensity coupling [15, 18]. The experiment

presented in this work differs from previous experiments in that it demonstrates PI for a 28.188 kHz acoustic mode with an effective (modal) mass of 0.125 kg in a suspended cavity apparatus. The mass and frequency regime of this experiment are of particular interest to GW detectors and ponderomotive squeezing experiments [19]. Moreover, we demonstrate that the PI may be stabilized by locking the laser frequency to the cavity mode, an important result for any experiment under threat of PI, such as Advanced LIGO [20].

1.2 Outline

In the following chapter, we present a unified model describing the coupling of an optical field to a classical harmonic oscillator. Before the model is presented, we review the basic properties of Fabry-Perot cavities, including a derivation of the power gain, finesse, and linewidth, and discuss the classical electrodynamics of radiation pressure. The unified model is approached via examination of the frequency domain equation of motion for a mirror, and we show that the system is well described using concepts from control theory. The model is applied to the cases of the OS, whereby the optical rigidity dominates the mechanical rigidity, and to the PI, in which the velocity-dependent optical force creates an instability of a mechanical mode.

This work describes two different radiation pressure experiments performed during the 2005-2006 academic year. In Phase 1 (P1), we used two 250 g mirrors. The input mirror had a transmission of $T_1 = 0.64\%$ and the end mirror had a transmission of $T_2 \approx 10$ ppm. For our Phase 2 (P2) cavity, we replaced the input mirror with one with lower transmission ($T_1 = 0.08\%$), which yielded a higher finesse, and the end mirror with a small 1 g mirror, to “amplify” the optomechanical dynamics, mounted on a larger steel shell. The physical specifications and parameters for the P1 and P2 cavities can be seen in Table 3.1.

In Chapter 3 we describe the apparatus as well as the control and measurement systems used to probe and characterize the system. We describe the mechanical configuration of the mirrors, consider the system block diagram and solve for the

loop gain. In Chapter 4 we describe our observations; we measure the strength of the PI as a function of cavity power and detuning, and demonstrate its control. We measure the loop gain of the system, and use it to characterize the features of the OS, including its instability, and suppression of noise forces. Lastly, we discuss the approach towards a quantum limited regime, and describe steps that may be taken to get there.

Chapter 2

Theory of Radiation Pressure Effects

In this chapter we present a theoretical model for the radiation pressure effects we observed. Before the model is presented, however, we find it beneficial to review the properties of Fabry-Perot interferometers and the physics of radiation pressure forces. From there, we shall be equipped to describe the two principal effects we observe: namely, the optical spring effect (OS), and the parametric instability (PI).

2.1 Fabry-Perot basics

In this work we experimentally demonstrate radiation pressure effects on the mechanical motion of mirrors suspended in Fabry-Perot cavities. Before discussing these radiation pressure effects, we present a review of the properties of Fabry-Perot optical cavities.

A diagram of the fields and optics associated with our Fabry-Perot cavity is shown in Figure 2-1. Fabry-Perot cavities have found wide use in both experimental physics and engineering applications since their initial development in the early twentieth century. For spectroscopy and astronomical applications, the device is generally called the Fabry-Perot étalon and has fixed mirrors. A Fabry-Perot interferometer is one in which the mirrors are movable, allowing the cavity to be tuned to resonate at the

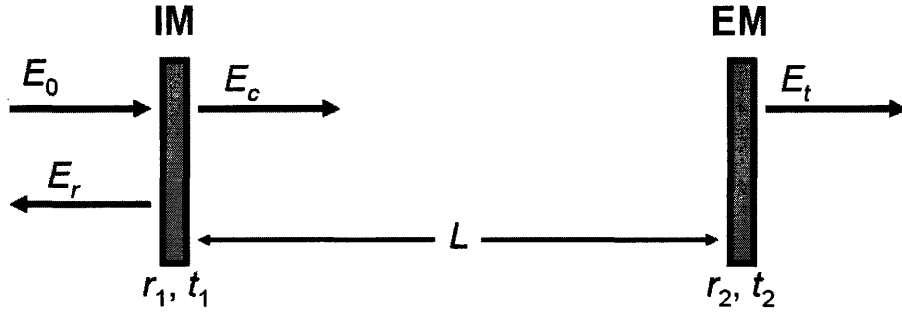


Figure 2-1: Optical fields and mirror parameters for the Fabry-Perot cavity.

incident laser frequency.

The basic idea is that coherent light is incident on a partially transmitting Input Mirror (IM), enters the cavity, and bounces off a nearly completely reflective End Mirror (EM). As the transmission of the IM is lowered, the light stays inside the cavity for many more bounces, and the cavity can store a great deal of power. For a fixed wavelength of the light λ_0 , the stored power is resonantly enhanced when the cavity length L is a half-integer multiple of λ_0 , corresponding to constructive interference. We determine the power resonances by first computing all the optical fields in the cavity and calculating the stored power as a function of the round-trip phase ϕ .

To determine the power storage as a function of frequency ω_0 (or equivalently, wavelength λ_0 , length L , or phase shift ϕ), we consider the relations between the fields at the mirror surfaces. From the field definitions in Figure 2-1, we desire expressions for the reflected field E_r , transmitted field E_t , and internal cavity field E_c as a function of the incident field E_0 , mirror amplitude reflectivities r_1 and r_2 , and mirror amplitude transmission coefficients t_1 and t_2 .¹ We begin with a recursively defined definition for E_c , consider the components transmitted through the IM and re-reflected off the EM and IM again. We assume that all laser fields are monochromatic plane waves, travelling along the z axis with the form $\exp[i(kx - \omega_0 t)]$ over the beam profile of

¹As in [21], we take the amplitude reflection and transmission coefficients to be real without loss of generality. The sign flips from reflection off of mirror coatings takes care of the phase changes.

area A . We find that

$$E_c = t_1 E_0 + e^{i\phi}(-r_1)(-r_2)E_c, \quad (2.1)$$

which yields, upon simplification,

$$E_c = \frac{t_1 E_0}{1 - r_1 r_2 e^{i\phi}}. \quad (2.2)$$

With the cavity field E_c in hand, finding the reflected and transmitted fields is simple:

$$E_r = r_1 E_0 + (t_1)(-r_2)E_c e^{i\phi} = \frac{1 - r_2 e^{i\phi}}{1 - r_1 r_2 e^{i\phi}} E_0 \quad (2.3)$$

$$E_t = t_2 E_c e^{i\phi/2} = \frac{t_1 t_2 e^{i\phi/2}}{1 - r_1 r_2 e^{i\phi}} E_0, \quad (2.4)$$

where $T_1 = t_1^2$.

As we now know the internal cavity field, we can compute the stored power as

$$W(\phi) = |E_c|^2 = \frac{T_1 E_0^2}{(1 + R_1 R_2) - 2r_1 r_2 \cos \phi}. \quad (2.5)$$

From Eq. (2.5), we find that the cavity is resonant whenever $\phi = 2\pi n$ for integer n , or, in terms of the wavelength and cavity length,

$$L = \frac{n\lambda_0}{2}, \quad (2.6)$$

from which we understand that the cavity moves through two power resonances for each change in cavity length ΔL of λ_0 . This can also be quantified in terms of frequency; the angular frequency difference between two adjacent power resonances is the Free Spectral Range (FSR) $\Delta\omega$ of the cavity,

$$\Delta\omega = \frac{\pi c}{L}. \quad (2.7)$$

We plot $W(\phi)$ in Figure 2-2. The FSR is the phase (or frequency difference) between adjacent power resonances.

Our experiments operate in a regime in which Eq. (2.5) can be simplified signifi-

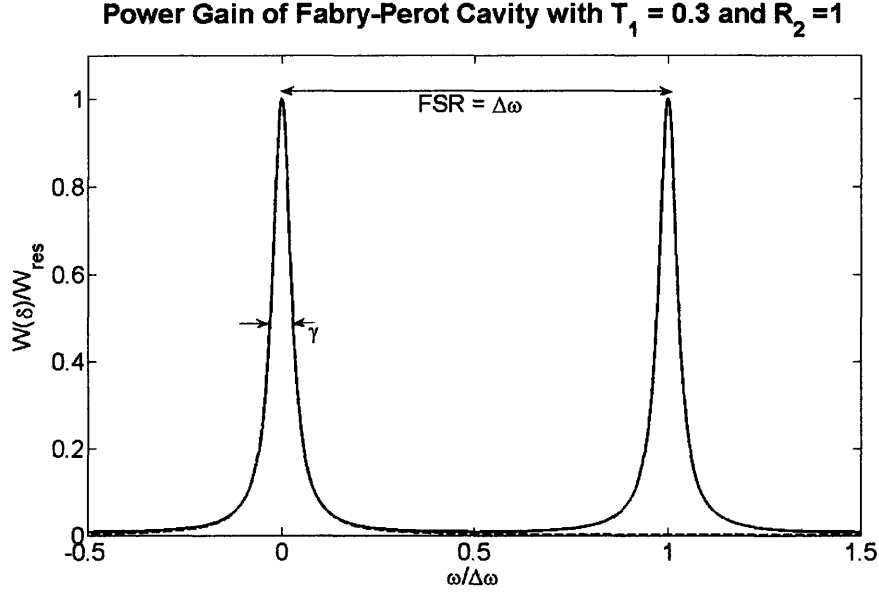


Figure 2-2: Analytical and Lorentzian approximations to the cavity power storage $W(I_0, \delta_\gamma)$ for a cavity with IM power transmission of 0.3 and EM reflectivity of 1.

cantly, giving analytical expressions for the linewidth of the cavity in terms of mirror properties and other parameters. We use a nearly perfectly reflective end mirror ($T_2 \approx 10$ ppm), and all mirrors have total scattering and absorption losses $L < 100$ ppm. As all mirrors obey the energy conservation identity

$$T + R + L = 1, \quad (2.8)$$

we approximate $R_2 = 1$ and $R_1 = \sqrt{1 - T_1}$. Also, we operate our cavities very close to resonance, such that the phase shift, which has unique values only in the range $[0, 2\pi)$, always takes values $\phi \ll 1$. Making these approximations, a single resonance peak is approximated by a Lorentzian. This is shown in Figure 2-2, where the solid curve is a plot of Eq. (2.5) and the dashed curve is a Lorentzian with linewidth γ computed by solving

$$\frac{W(\phi = 0)}{2} = \frac{T_1 E_0^2}{2 - T_1 - 2\sqrt{1 - T_1} \cos(2\gamma L/c)} \Rightarrow \gamma = \frac{cT_1}{4L}. \quad (2.9)$$

The finesse of a Fabry-Perot is defined as the ratio between the FSR and the linewidth,

$$\mathcal{F} = \frac{\Delta\omega}{\gamma} = \frac{2\pi}{T_1}. \quad (2.10)$$

The finesse of a cavity is a measure of the frequency discrimination of the cavity in spectroscopy applications, and is analogous to the quality factor Q of mechanical oscillators. Specifically, our P2 cavity used an IM transmission of $T_1 = 800$ ppm, which yields a finesse of $\mathcal{F} \approx 8000$.

In discussing radiation-pressure effects we shall frequently talk about Fabry-Perot cavities in states detuned from resonance. We introduce the detuning parameter

$$\delta = \omega_0 - \omega_{\text{res}} = \omega_0 - \frac{\pi cn}{L}. \quad (2.11)$$

This quantity is useful, but we prefer a dimensionless detuning normalized by the linewidth,

$$\delta_\gamma = \frac{\delta}{\gamma} = \frac{cT_1}{4L} (\omega_0 - \omega_{\text{res}}). \quad (2.12)$$

We also define the input intensity as $I_0 = E_0^2$. We can cast our power storage formula $W(\phi)$ into an equation for $W(I_0, \delta_\gamma)$. We find that

$$W(I_0, \delta_\gamma) = \frac{4I_0}{T_1} \frac{1}{1 + \delta_\gamma^2}, \quad (2.13)$$

which is a Lorentzian distribution with a linewidth of 1.

2.2 Radiation Pressure forces

According to classical electrodynamics, electromagnetic fields in vacuum have a momentum density

$$\vec{\wp} = \frac{1}{c^2} \vec{S} \quad \text{where} \quad \vec{S} = \frac{1}{\mu_0} (\vec{E} \times \vec{B}), \quad (2.14)$$

the Poynting vector, describes the power delivered by the fields per unit area [22]. Assuming the laser beams inside the cavity are monochromatic plane waves of the

form $\vec{E} = E_0 e^{i(kz - \omega_0 t)} \hat{x}$ over the beam size, we have that the time averaged momentum density $\langle \vec{\rho} \rangle$ is

$$\langle \vec{\rho} \rangle = \frac{1}{2c} \epsilon_0 E_0^2 \hat{z}. \quad (2.15)$$

If we assume the beam has area A and strikes a perfectly reflective mirror, it will impart

$$\Delta \vec{p} = 2 \langle \vec{\rho} \rangle A c \Delta t \quad (2.16)$$

during some time interval Δt . From (2.16) we can calculate the force on the mirror,

$$\vec{F} = \frac{\Delta \vec{p}}{\Delta t} = \epsilon_0 A E_0^2 \hat{z} = \frac{2W}{c} \hat{z} \quad (2.17)$$

where W is the total intracavity power. The second simplification comes from the interpretation of the magnitude of the Poynting vector $|\vec{S}| = \epsilon_0 E_0^2$ as the power per unit area striking the mirror. The radiation pressure force \vec{F} will fluctuate with whatever fluctuations are inherent in W due to passage of the cavity through resonances via either length or laser frequency changes.

2.3 Unified Model of Optical Rigidity

In the cavities we explore experimentally, our IM and EM are suspended as pendulums in a vacuum chamber. Performing the experiment in vacuum reduces susceptibility to acoustic noise and air currents, and the pendulum provides isolation to some ground noise. However, the fact that the mirror is free to move, rather than fixed to a table, is a crucial component of our experiment. Here we discuss the dynamics of a generic mechanical oscillator in the presence of the laser light.

We build our model gradually. We first consider quasistatic motion, where the angular frequency $\Omega \ll \gamma$, and determine the resulting radiation pressure force, defining the DC rigidity K_0 . We then consider dynamical shifts of the cavity length, and consider the complete equation of motion of the cavity, and discuss an intuitive feedback model to represent it.

To simplify our discussion, we assume only one mirror is free to move. In addition, we separate any dynamical variable into a sum of its mean (DC) component and small-amplitude fluctuations about this point; for example $x = \bar{x} + \tilde{x}$, where \bar{x} is the mean value of x and \tilde{x} are fluctuations about that mean.

2.3.1 Quasistatic Motion

We begin with a description in terms of the bulk pendular motion of the mirrors; all the relevant physics is generic to any oscillator but the concepts are more easily grasped in the context of a specific system. Suppose the cavity is sitting on a resonance; this means that there is a DC radiation pressure (or ponderomotive) force F acting on the mirror with magnitude

$$F = \frac{2W(I_0, \delta_\gamma = 0)}{c}. \quad (2.18)$$

Let us then consider what happens when we slowly move the mirror to a distance \bar{x} from the resonance position, and consider fluctuations \tilde{x} . The static detuning $\bar{\delta} = \Delta\omega(\bar{x}/L)$ causes the cavity causes the stored power to change, which results in a fluctuating force \tilde{F} . Therefore, \tilde{F} will consist of two parts: one resulting from the restoring force of the pendulum, and one resulting from the ponderomotive force:

$$\tilde{F} = - \left(M\Omega_p^2 + \frac{2}{c} \frac{\partial W(I_0, \bar{\delta}_\gamma)}{\partial \bar{\delta}_\gamma} \frac{d\bar{\delta}_\gamma}{dx} \right) \tilde{x}, \quad (2.19)$$

where Ω_p is the resonant frequency of the pendulum. This equation will be valid for mirror motions at frequencies $\Omega \ll \gamma$. This is fairly easily understood: γ^{-1} represents the cavity response time – the amount of time it takes for the cavity power to adjust to a change in length. Therefore, as long as the mirror motions \tilde{x} are negligible on this time scale, the motion is quasistatic, and Eq. (2.19) is valid.

We now attempt to evaluate the optomechanical force, seen as the rightmost term in Eq. (2.19). To evaluate $d\bar{\delta}_\gamma/dx$ we treat L as the length variable and differentiate

Eq. (2.12), finding

$$\frac{d\bar{\delta}_\gamma}{dx} = \frac{4\omega_0}{cT_1}. \quad (2.20)$$

We find $\partial W/\partial\bar{\delta}_\gamma$ by differentiating (2.13). Combining these expressions, we find that

$$\frac{2}{c} \frac{\partial W(I_0, \bar{\delta}_\gamma)}{\partial\bar{\delta}_\gamma} \frac{d\bar{\delta}_\gamma}{dx} = -\frac{64\omega_0 I_0}{c^2 T_1^2} \frac{\bar{\delta}_\gamma}{(1 + \bar{\delta}_\gamma)^2}. \quad (2.21)$$

The overall negative sign tells us that when $\bar{\delta}_\gamma > 0$ the ponderomotive force has given an additional restoring force characterized by the spring constant

$$K_0 = \frac{64\omega_0 I_0}{c^2 T_1^2} \frac{\bar{\delta}_\gamma}{(1 + \bar{\delta}_\gamma)^2}. \quad (2.22)$$

The fact that an additional optical restoring force arises is not surprising: detuning the cavity further from resonance creates a power deficit which the cavity tries to correct for by shortening its length. From this, we can define a characteristic optical spring frequency

$$\Theta \equiv \sqrt{\frac{K_0}{M}} = \frac{8}{T_1} \sqrt{\frac{2\pi I_0}{c\lambda_0 M}} \frac{\sqrt{\bar{\delta}_\gamma}}{1 + \bar{\delta}_\gamma^2}, \quad (2.23)$$

where M is the mass of the suspended mirror. We note that the detuning can take both positive and negative values, depending on whether the cavity is blueshifted ($\bar{\delta} > 0$) or redshifted ($\bar{\delta} < 0$). As is seen in Figure 2-3, a blueshifted cavity produces a Hooke's Law restoring force for fluctuating $\bar{\delta}_\gamma$ as $W(I_0, \delta_\gamma)$ has an approximately constant negative slope; in this case Θ is a real, positive number. A redshifted cavity, however produces an anti-restoring force and Θ is purely imaginary, corresponding to cold damping.²

The static detunings $\bar{\delta}_\gamma = \pm\sqrt{3}/3$ correspond to the maximum or minimum K_0 found by differentiating Eq. (2.22) with respect to $\bar{\delta}_\gamma$ and setting the result to 0. This optimal detuning corresponds to a stored power $W(I_0, \bar{\delta}_\gamma = \sqrt{3}/3) = \frac{3}{4}W(I_0, \bar{\delta}_\gamma = 0)$.

²We use the sign convention in which positive detunings produce an optical spring. If δ is defined as $\omega_{\text{res}} - \omega_0$ as in [19], *delta* < 0 will correspond to an optical spring

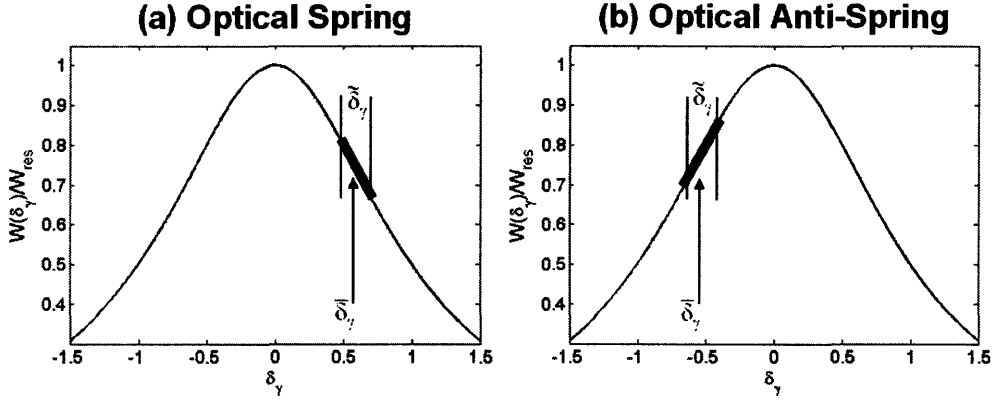


Figure 2-3: Illustration of differing optomechanical dynamics depending on the sign of the detuning δ_γ . In (a), positive δ_γ gives a restoring force, whereas in (b) the negative δ_γ gives an anti-restoring force.

2.3.2 Frequency Domain Feedback Description

We now discuss an approximation to a dynamic equation of motion for any mechanical mode of the mirror, and intend to include terms related to delayed cavity response. Again, we only discuss fluctuation terms, and assume that DC radiation pressure effects are controlled by our actuators, which will be discussed in Chapter 3. We begin with the time domain equation of motion and include the environmental and applied force \tilde{F}_a ,

$$M \frac{d^2 \tilde{x}}{d\tilde{x}^2} = - (M\Omega_p^2 + K_0) \tilde{x} + \frac{M\Omega_p}{Q} \frac{d\tilde{x}}{dt} + \tilde{F}_a, \quad (2.24)$$

where Q is the quality factor of the mechanical oscillations. In order to account for cavity delays we introduce a frequency dependence in the optical rigidity, i.e. $K_0 \rightarrow K(\Omega)$. We transform Eq. (2.24) into the frequency domain by putting $d/dt \rightarrow i\Omega$,

$$-\Omega^2 \tilde{x} = - \left(\Omega_p^2 + \frac{K(\Omega)}{M} + \frac{i\Omega\Omega_p}{Q} \right) \tilde{x} + \frac{\tilde{F}_a}{M}. \quad (2.25)$$

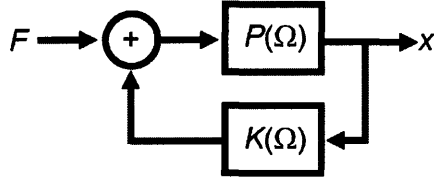


Figure 2-4: Representation of the optical rigidity as a feedback system.

From this expression, we solve for the susceptibility, or displacement per unit force as a function of frequency, of the oscillator when coupled to the optical field

$$P_{OR}(\Omega) = \frac{\tilde{x}}{\tilde{F}_a} = \frac{1/M}{-\Omega^2 + \Omega_p^2 + \frac{i\Omega\Omega_p}{Q} + \frac{K(\Omega)}{M}}. \quad (2.26)$$

This expression, however, is cumbersome, and we demonstrate a more intuitive approach to the effect of the optical coupling.

The form of the susceptibility in Eq. (2.26) can be shown to be algebraically equivalent to the expression

$$P_{OR}(\Omega) = \frac{P(\Omega)}{1 - P(\Omega)K(\Omega)} \quad (2.27)$$

where $P(\Omega)$ is the mechanical susceptibility of the mechanical mode in the absence of optical coupling,

$$P(\Omega) = \frac{1/M}{-\Omega^2 + \Omega_p^2 + i\Omega\Omega_p/Q}. \quad (2.28)$$

The reader familiar with basic control theory will recognize Eq. (2.27) as the transfer function of the feedback system shown in Figure 2-4. The description of the optical rigidity effect via feedback systems provides an intuitive description of the physical processes involved. An input force is converted into a displacement by the mechanical oscillator. This displacement, however, is converted back into a force by the optical rigidity, which again drives the oscillator.

For optomechanical coupling to occur in Fabry-Perot cavities via radiation pressure, some mechanism must linearly couple the phase fluctuations induced by mechanical motion to intensity fluctuations of the intracavity field. The mechanism we

use is to detune the laser frequency from the center of the cavity resonance, such that the stored power (and hence the radiation pressure force) has a linear dependence on the cavity length.

Once we have an expression for $K(\Omega)$, our model will be complete. The frequency dependence $K(\Omega)$ is due to the fact that power buildup, and therefore rigidity-induced force in the cavity, does not respond instantaneously to changes in cavity length. A derivation, valid for all $\Omega \ll \Delta\omega$ is given by Khalili and Vyatchanin [23]. They show that

$$K(\Omega) = -\frac{2i\omega_0^2|E_c|^2}{cL} \left[\frac{1}{\ell(\Omega)} - \frac{1}{\ell^*(-\Omega)} \right], \quad (2.29)$$

where the denominator $\ell(\Omega) = \gamma - i(\delta + \Omega)$. We include the $\ell(\Omega)$ terms to account for the creation of frequency sidebands due to the motion of the mirror. Mirror motion at Ω causes phase modulation of the carrier light, which is mathematically equivalent to the creation of sideband fields at $\omega_0 \pm \Omega$. The inclusion of $\ell(\Omega)$ places poles in $K(\Omega)$ at the sideband frequencies $\gamma \pm \delta$. Upon simplification, Eq. (2.29) yields

$$K(\Omega) = K_0 \frac{1 + \bar{\delta}_\gamma^2}{\left(1 + \frac{i\Omega}{\gamma}\right)^2 + \bar{\delta}_\gamma^2}. \quad (2.30)$$

We note here that a real rigidity corresponds to a Hooke's law spring constant, where an imaginary rigidity corresponds to a viscous, velocity dependent force (which may be either damping or anti-damping, depending on whether its sign is negative or positive).

2.4 Optical Spring Effect and Noise Suppression

In our cavities, both mirrors are suspended. This does not, however add significant complexity to the dynamics; the relevant length simply becomes the distance between the two mirrors, and we can replace the mass M by the reduced mass $\mu = M_I M_E / (M_I + M_E)$ where M_I and M_E are the masses of the IM and EM respectively.

If the mechanical mode under consideration is the pendulum mode of the mirrors, we have $\Omega_p = 2\pi \times 1$ Hz, and in general $K(\Omega) \gg \mu\Omega_p^2$. If, in addition, we restrict ourselves to frequencies $\Omega \ll \gamma$, we can expand $K(\Omega)$ in a Taylor series to first order in Ω/γ , and have

$$K(\Omega) \approx K_0 \left(1 - \frac{2i\Omega}{\gamma} \frac{1}{1 + \bar{\delta}_\gamma^2} \right). \quad (2.31)$$

With this simplification, we can express $P_{OR}(\Omega)$ in the same form as the pendulum susceptibility $P(\Omega)$ with a modified resonant frequency

$$\Omega_p'^2 = \Omega_0^2 + \frac{K_0}{\mu} \approx \Theta^2 \quad (2.32)$$

and quality factor

$$Q' = -\frac{\gamma}{2\Theta} (1 + \bar{\delta}_\gamma^2). \quad (2.33)$$

We notice immediately that the modified Q' has become negative, corresponding to an anti-damping viscous optical force. Experimental signatures of this feature will be that the optical spring mode will ring up unless it is stabilized by feedback, and that the phase of the response will increase by 180° across the resonance.

For an example of how $P_{OR}(\Omega)$ is modified as the rigidity K_0 is increased, see the plots in Figure 2-5. Here, we plot the expected form of $P_{OR}(\Omega)$ for the parameters of the P2 cavity, in which $\Omega_p = 2\pi \times 171$ Hz and $\gamma = 2\pi \times 10$ kHz. Notice the broadening of the resonance peaks as K_0 increases and Θ moves to higher frequencies. These plots were made by a numerical solution to Eq. (2.27) in terms of $P(\Omega)$ and $K(\Omega)$, which holds for all frequencies and arbitrary $K(\Omega)$. The formulas in Eqns. (2.32) and (2.33) begin to break down as $\Theta \rightarrow \gamma$, as in this situation.

Another important feature of the optical rigidity is the suppression of force noises below the resonant frequency. Consider two systems: a Fabry-Perot cavity on resonance and one detuned from resonance. The response of the resonant cavity length to external forces applied to the mirrors is the pendulum susceptibility, which is flat for $\Omega < \Omega_p$ and falls like $1/\Omega^2$ for frequencies $\Omega > \Omega_p$. For the detuned cavity, if we consider frequencies $\Omega < \Theta$, we notice that the displacement sensitivity to external

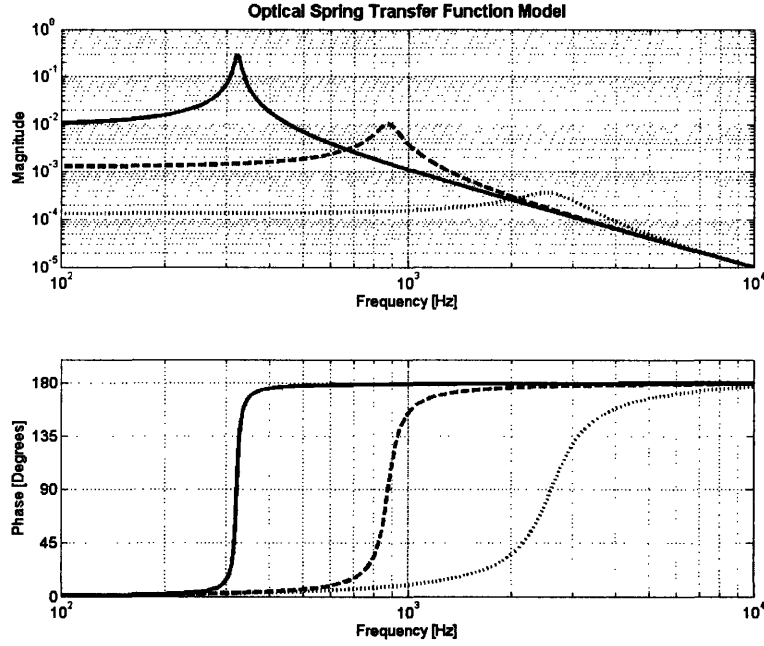


Figure 2-5: Numerical calculation of $P_{OR}(\Omega)$ based on Eq. (2.27) for Phase 2 cavity parameters and three values of K_0 .

forces is given by

$$\tilde{x} = \frac{\Omega^2}{\Omega^2 - \Theta^2} \tilde{x}_0 \quad (2.34)$$

where \tilde{x}_0 is the displacement of the resonant cavity. The noise suppression effect can be viewed in the model data of Figure 2-5 as the lowering of the magnitude of $P_{OR}(\Omega)$ at low frequencies. Our experimental design puts us in a regime where Θ can exceed Ω_p by nearly three orders of magnitude, resulting in a million-fold suppression of mirror displacement due to force noise at low frequencies. This noise suppression feature of our optical spring is a crucial feature of interferometers designed to produce squeezed light via ponderomotive coupling [19].

An important point to consider is why an optical spring more desirable than a much stiffer mechanical oscillator. The key difference is that the thermal noise entering the system can increase with the strength of the oscillator; optical rigidity, by its nature, adds no thermal noise.

2.5 Parametric Instability

Our discussion of radiation-pressure induced dynamics has so far been concerned only with bulk longitudinal motion of the pendulum mode of the mirror. However, we can apply the same expressions to any mirror mode which can affect cavity length. The optical spring effect, altering the pendulum resonance, is the primary physical effect at frequencies at or below γ . For mirror motions at frequencies $\Omega \gtrsim 2\pi \times 10$ kHz, the primary mirror mode of interest is the drumhead acoustic phonon mode of the mirror.

The drumhead mode for our 250 g mirror has been measured to be at $\Omega_d = 2\pi \times 28.188$ kHz. The effective (or modal) mass for this mode, M^* , will not necessarily be the same as the mirror mass, and shall have to be determined experimentally. The mirror has many other acoustic modes, but other than the lowest order drumhead mode none have the proper spatial or spectral overlap with the cavity laser mode to affect the dynamics of the system.

In this higher frequency regime, the mechanical restoring force provided by the drumhead mode is much larger than the optical restoring force, or $\Omega_d^2 \gg K_0/M^*$, so the resonant frequency of the mechanical mode will be unchanged. However, as we saw above, if the quality factor of the mode and the optical rigidity are large enough, the Q' will become negative and an instability will result. We define the instability factor, or susceptibility, R , as the gain of the optomechanical feedback loop. It is estimated by considering the product of two factors; first, it includes the response (displacement/force) of the mirror surface to forces at the resonant frequency $Q/(M^*\Omega_d^2)$. The second term we include is the viscous radiation pressure force per unit displacement exerted by the optical field due to the motion of the mirror. As we use a complex-valued rigidity, the imaginary component $\text{Im}[K(\Omega_d)]$ gives this viscous damping constant. R is thus estimated by

$$R \approx \frac{\text{Im}\{K(\Omega_d)\}Q}{M^*\Omega_d^2}. \quad (2.35)$$

When $R > 1$, the modified Q' is negative, and the oscillations are unstable. When

$R < 1$, Q' is positive, and the oscillations become damped. The unified model gives similar results to that of Braginsky et al. [17], who first defined the dimensionless PI susceptibility, R . Still, however, the result is an approximation. For theoretical curves of R versus detuning presented in Chapter 4, we calculate R by numerically solving the equation of motion.

We have not discussed the physical processes involved in this instability; they are subtle but can be understood by considering the phase-modulation sidebands created by the mirror motion. Oscillations of a mirror mode of frequency Ω_m cause phase modulation of the carrier light inside a cavity, creating a pair of sidebands centered at $\omega_0 \pm \Omega_m$. In general, the cavity may have an asymmetric optical response to these sidebands, so one may build up in intensity at a faster rate than the other. The imbalance in these sidebands results in fluctuating amplitudes of the light, and therefore oscillating radiation pressure forces. Depending on which sideband is favored, one of two results can happen:

1. The upper sideband (anti-Stokes mode) is favored, resulting in damping of the mechanical mode.
2. The lower sideband (Stokes mode) is favored, resulting in a run-away scenario in which the drumhead mode is resonantly driven by the amplitude fluctuations at a rate faster than energy is removed by the anti-Stokes mode removes energy.

Situation 2 is the Parametric Instability, PI, that we hope to measure in our experiment. As with the OS, it occurs only for positive δ . Its signatures will be that the strength of the PI, as characterized the the ringup time of the 28 kHz drumhead mode, will be dependent on the cavity power and detuning, and should only occur on one side of the resonance, where the Stokes mode is favored.

Chapter 3

Apparatus and Control Systems

In the last chapter, we discussed several radiation pressure effects that can be observed in Fabry-Perot optical cavities. In the present chapter, we discuss our apparatus and technique by which we hope to measure and characterize the Optical Spring (OS) and Parametric Instability (PI). We also discuss the electronics and control systems needed to stabilize the system and lock the Fabry-Perot cavity.

As was mentioned in Chapter 1, we performed radiation experiments on two different cavities. The properties of the P1 and P2 cavities are shown in Table 3.1.

3.1 Experimental Setup

A top-level schematic of our experimental setup is shown in Figure 3-1. The Fabry-Perot cavity consists of two mirrors suspended as pendulums. The cavity is placed in a good quality vacuum of 10^{-6} Torr to reduce the effects of acoustic force noises. The vacuum chamber sits on the same HEPI active seismic isolation system that is used in the LIGO interferometers. Unfortunately, the HEPI system was down for maintenance and further research during the running of our experiment. Even so, we found that by running our experiments at night when street noise was reduced we were not hampered too much by ground noise.

The light injected into the cavity is first passed through a quarter-wave plate so as to rotate the polarization, causing the reflected beam to be picked off at the

Parameter	Symbol	P1 Value	P2 Value	Units
IM Transmission	T_1	6400	800	ppm
EM Transmission	T_2	10	10	ppm
Cavity Length	L	1.0	0.9	m
FSR	$\Delta\omega$	0.94	1.04	GHz
Cavity Linewidth	γ	$2\pi \times 76.1$	$2\pi \times 10.6$	kHz
Finesse	\mathcal{F}	982	7850	
IM Mass	M_1	250	250	g
EM Mass	M_2	250	1	g
		Single 1 Hz	Composite 1 Hz	
EM Suspension		Pendulum	Pendulum and 179 Hz Fiber Mount	

Table 3.1: P1 and P2 cavity parameters, symbols, and values.

beamsplitter. This light is needed to provide a signal for our two feedback loops. For low frequency control, we have an actuation mechanism for controlling the length of the cavity via inductive forces on magnets glued onto the mirrors. For high frequency control, we modulate the laser frequency with a Voltage Controlled Oscillator (VCO).

3.1.1 Damping Control

To precisely control the positions and angles of each mirror with respect to its suspension tower, we use the OSEM (Optical Sensor and ElectroMagnetic actuator) used to control the small optics in LIGO. Five permanent magnets are glued onto the each optic: one is placed on the side (S), and four are on the back in a square pattern (UR, UL, LL, LR). Situated behind each of these magnets is a small loop of wire and and LED and small photodiode. The position of the mirror is read by the amount of light hitting each photodiode; as the mirror moves towards the OSEM, a shadow is created and the amount of light reaching the photodiode is diminished. Each of the five OSEM signals $x_i(t)$ where $i \in \{UR, UL, LR, LL, S\}$ are re-interpreted into the four degrees of freedom we control:

1. Longitudinal position along the beam path: $S_l(t) = x_{UR} + x_{UL} + x_{LL} + x_{LR}$
2. Mirror pitch: rotation about a horizontal axis through the center of mass:

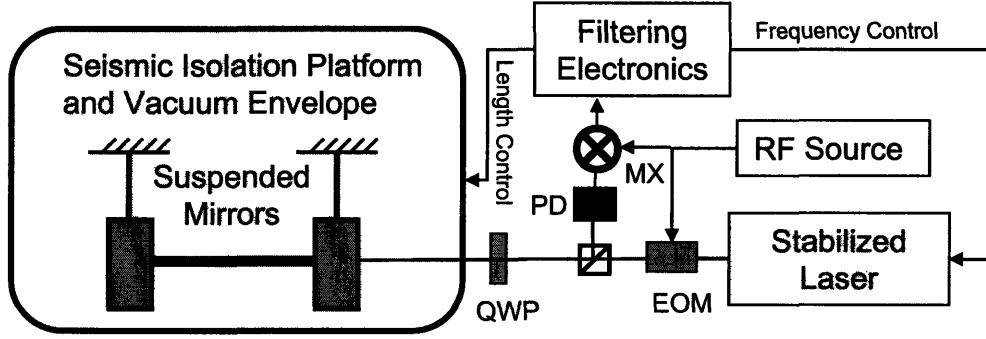


Figure 3-1: Schematic representation of the experiment. Approximately 5 W of intensity- and frequency-stabilized 1064 nm Nd:YAG laser light is incident on a Fabry Perot cavity. EOM refers to electrooptic modulator; MX to mixer; PD to photodetector; and QWP to quarter-wave plate.

$$S_p(t) = (x_{UR} + x_{UL}) - (x_{LL} + x_{LR})$$

3. Mirror yaw: rotation about a vertical axis through the center of mass: $S_y(t) = (x_{UR} + x_{LR}) - (x_{UL} + x_{LL})$
4. Side-to-side motion of mirror perpendicular to the beam path: $S_s(t) = x_s$.

The signals S representing the position coordinate for each degree of freedom are voltages in the range $-2 < S < 0$ V. The control system uses a velocity damping mechanism to suppress motion in each of the degrees of freedom. Using standard analog circuitry, each signal S is differentiated, inverted, and fed back with gain only at frequencies lower than $f \lesssim 2$ Hz to damp out the resonant longitudinal, pitch, and yaw modes at 1, 0.6, and 0.5 Hz, respectively. To actuate on the mirrors, a current proportional to the mirror position is driven through the coils, producing a time-dependent magnetic field that attracts or repels the corresponding mirror magnet.

3.1.2 Interferometric Sensing and Control

The OSEM system provides only local damping. The optical sensors only detect the motion of the nearby mirror with respect to the suspension tower, and the damping control process only affects the low frequency resonant motions of the mirrors.

To lock the cavity, a signal proportional to the cavity length must be acquired and analyzed. Pound-Drever-Hall (PDH) interferometric sensing and control is used to lock the cavity. The laser light is passed through an electrooptic modulator (or Pockels cell), which phase-modulates the carrier beam and produces a pair of RF sidebands at $\omega_0 \pm 2\pi \times 25.2$ MHz. The sidebands are designed to be far off resonance so that the sideband fields are reflected off the cavity and are used as a phase reference.

Before entering the cavity, the phase-modulated light is passed through a beamsplitter and a quarter-wave plate. This ensures that the polarization of the reflected light has been rotated, so it will deflect at the beamsplitter and strike the photodiode. The photodiode signal is demodulated with the same RF source, producing the PDH error signal which provides the required information necessary to control the laser frequency. We have two actuation mechanisms by which the cavity can be locked to the laser; the length and frequency control mechanisms are discussed below.

Length Control

We first consider the length path; the PDH error signal $e(\Omega)$ is passed through an electronic filter $H_L(\Omega)$, the shape of which can be seen in Figure 3-2. It is important to note, however, that the transfer function $H_L(\Omega)$ does not directly give the mirror displacement as a function of frequency. We need to understand a bit more of the dynamics of the system in order to obtain the frequency dependence of our length control system. The error signal for the mirror position is defined as $e(t) \equiv S_l(t) - S_{\text{app}}(t)$, so it is the difference between our applied signal and the mirror motion, and is a measure of the residual motion of the cavity. However, due to the finite response time of the cavity, we are not sensitive to very high frequency components of the error signal. The cavity transfer function $C_P(\Omega)$ is introduced to reflect this fact; it consists of a pole at $\Omega = \gamma$:

$$C_P(\Omega) = \frac{1}{i\Omega/\gamma + 1}. \quad (3.1)$$

To provide the length control, we use the same magnetic actuators as in the damping control system. Due to the pendulum response of the mirror, the displace-

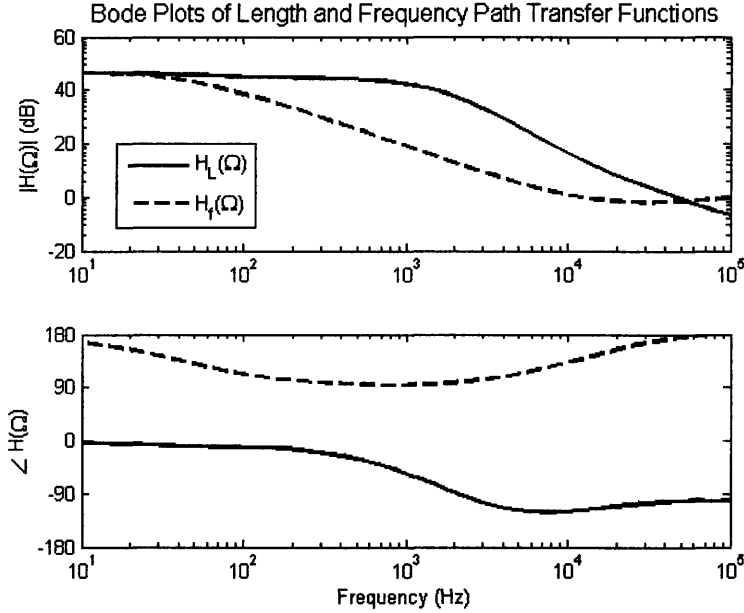


Figure 3-2: Electronic length and frequency control transfer functions $H_L(\Omega)$ and $H_f(\Omega)$. The overall scaling is adjustable, and the frequency dependence of the sensing and length actuation mechanisms is not accounted for.

ment/force transfer function of the mirror is not flat. Rather, the mirror has a frequency response

$$P(\Omega) = \frac{1/M}{-\Omega_p^2 + i\Omega\Omega_p/Q + \Omega_p^2}. \quad (3.2)$$

where Q is the quality factor of the pendulum oscillations, and Ω_p is the resonant frequency. For simplicity, we assume that the actuation mechanism for converting a voltage into a force is flat. The system interconnections can be seen in Figure 3-5. With all the components in place, the true sensing to mirror displacement transfer function is

$$L(\Omega) = G_L C_P(\Omega) H_L(\Omega) P(\Omega) \quad (3.3)$$

where G_L is an adjustable overall gain and $L(\Omega)$ is dimensionless.

In addition to the active feedback, the system allows us to control the DC position and orientation of the mirrors. This allows a very simple means to control the alignment of the optical cavity. In addition, particularly in the P2 cavity, the magnetic actuator allows a cancellation of the DC ponderomotive force due to the high cavity

circulating power. In addition, it is a DC current applied to the position that allows us to precisely detune the cavity to explore the dependence of the optical rigidity on the detuning.

Frequency Control

The laser is both intensity and frequency stabilized via feedback systems to produce a very stable nearly monochromatic beam at $\lambda_0 = 1064$ nm. Frequency control is done via the same actuator that stabilizes the laser.

The frequency control transfer function $H_f(\Omega)$ is plotted along with $H_L(\Omega)$ in Figure 3-2. Again due to the cavity pole, our sensing ability falls off as $1/\Omega$ for $\Omega > \gamma$. Unlike the length path, however, the frequency control actuator – the VCO acting on the laser frequency – has a flat frequency response. Therefore the sensing to control transfer function for frequency control is

$$F(\Omega) = G_f C_P(\Omega) H_f(\Omega) \quad (3.4)$$

where G_f is an adjustable overall gain.

Length-Frequency Crossover

A plot of $F(\Omega)$ and $L(\Omega)$ for typical G_L and G_f is shown in Figure 3-3. By selecting G_L and G_f , we set two important frequencies. The first of these, Ω_c , is defined by $F(\Omega_c) = L(\Omega_c)$. Thus, Ω_c is the length-frequency crossover frequency; at $\Omega < \Omega_c$, the length control path is dominant over the frequency control path, and therefore most of the work in maintaining lock is done via magnetic actuators. At $\Omega > \Omega_c$ the frequency control path is dominant, and most of the work is done by the VCO.

In addition, we note one other important frequency Ω_b , defined as the frequency at which the strongest control system gain crosses unity. We note that, by in large, $L(\Omega) \propto 1/\Omega^2$ and $F(\Omega) \propto 1/\Omega$, so $F(\Omega)$ is the dominant control system at high frequencies. The unity gain crossing specifies the maximum frequency at which our control system has the ability to modify the natural system dynamics. For this reason,

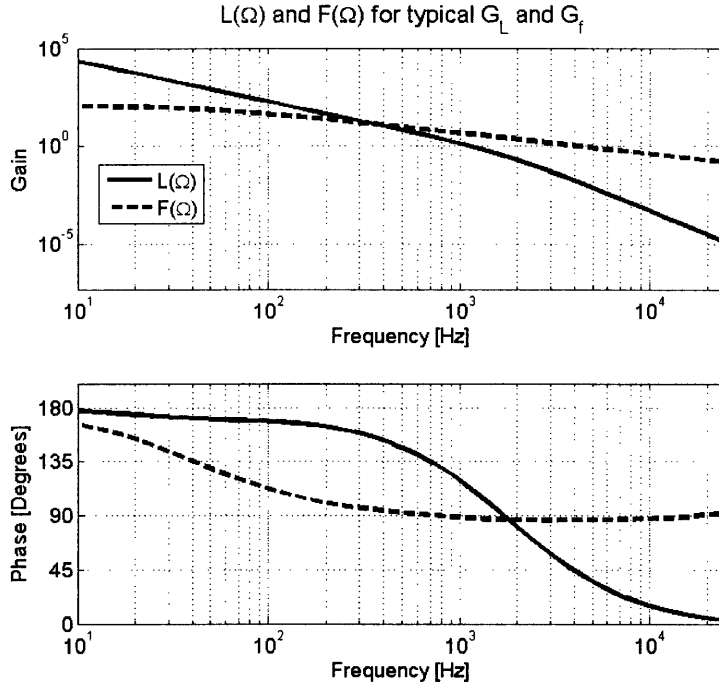


Figure 3-3: Plots of $L(\Omega)$ and $F(\Omega)$ for typical gains G_L and G_f , yielding crossover frequency $\Omega_c \approx 300$ Hz and locking bandwidth $\Omega_b \approx 4$ kHz.

we term Ω_b the locking bandwidth. It is important to keep the system's dynamical effects below the locking bandwidth so that any natural instabilities do not drive the cavity out of lock. For example, in our P2 cavity, the OS resonant frequency was made as high as $\Theta \approx 5$ kHz. In the previous chapter, we demonstrated the unstable nature of the OS effect, so in order to prevent a ringup of the OS, we must keep $\Omega_b > \Theta$.

Also note the relationship between the phases of $F(\Omega)$ and $L(\Omega)$. It is important that the two transfer functions never be near 180° out of phase at $\Omega \sim \Omega_c$, as in that case their effects would cancel. Rather, a 90° phase relationship enables proper control of the dynamics.

3.2 Mirrors and Suspensions

3.2.1 Phase 1: Large Optics

During Phase 1, we used two 250 g optics of the same dimensions as the LIGO small optics used in the input mode cleaners at the Hanford and Livingston observatories. The obvious benefit was that their optical and mechanical properties were already well understood. For example, several LIGO internal documents gave the frequencies of the acoustic modes of interest. In addition, the OSEM control system for optics of this size had already been designed and calibrated. Very little additional work needed to be done on the details of the length control mechanisms.

3.2.2 Phase 2: Composite EM

We seek to make the optical spring resonant frequency Θ as high as possible, to explore the strongest possible optomechanical coupling. As Θ scales like $1/\sqrt{\mu}$ for constant power and detuning, it is of experimental interest to use smaller masses. The problem that results is a similar length control system is much more difficult to implement. For Phase 2, we opted for a different system; rather than attempting to actuate directly on a small 1 g EM (with a radius of 0.7 cm), we mounted the small mirror onto a steel shell of the same size as the EM and IM used in P1. Strands of optical fiber were carefully glued to the sides of the small mirror, and these fibers were glued to the steel ring, as shown in Figure 3-4. After preparation for the vacuum chamber, magnets were glued on the steel ring in the same configuration used for larger optics.

The coupled oscillator presents more complicated dynamics. Finite element modelling of the composite mirror system gave a longitudinal resonant frequency of $\Omega_p \approx 30$ Hz. However, due to complications with the construction of the mirror,¹ the lowest frequency mode became $\Omega_p = 171$ Hz, with a pitch mode at $\Omega_{p2} \approx 350$ Hz.

¹To dry the glue used to fasten the fibers to the mini mirror and to the steel ring, the apparatus was placed in an oven and baked for several hours. Because the thermal expansion coefficient of the steel was approximately 10 times greater than that of the glass fibers, the glue set in a state in which the diameter of the ring had expanded more than a millimeter. Therefore, when the apparatus cooled, the fibers were bowed outwards and flexed. The longitudinal mode we now observe is a small perturbation on this bowed state, and has the 171 Hz resonant frequency.

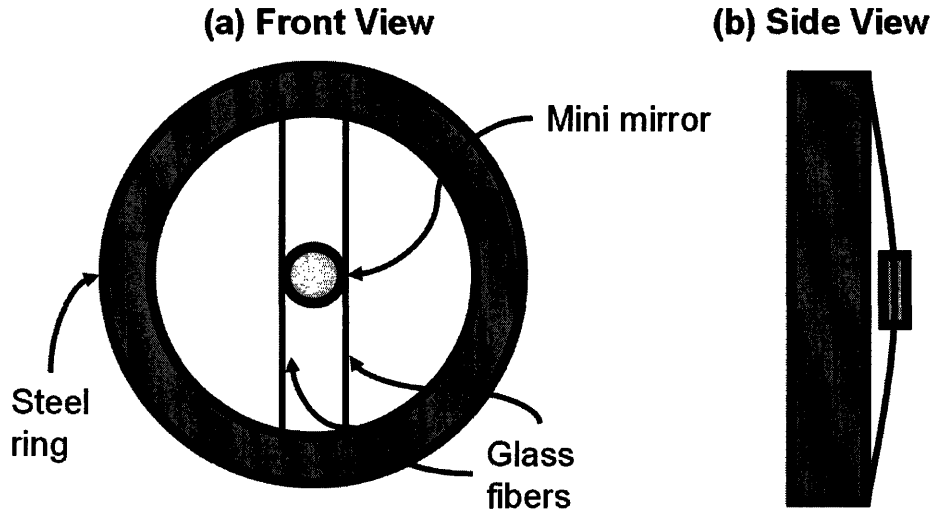


Figure 3-4: (a) Illustration of composite mirror and (b) fiber flexing effect due to thermal expansion.

The relative positioning of these modes makes sense with a corresponding physical picture: the pitch mode involves a second-order mode of the glass fiber with $k_{p2} = 2k_p$. Under the assumption that the fiber is nondispersive, the factor of two in frequency is logical.

3.3 Physics and Control System Simulation

Coupling the composite mirror to the laser initially produced some very counterintuitive results. To better understand the dynamics of the more complex optical system, a Simulink model of the optomechanical system, as well as the controls and readout system, was developed. This model was very useful as an experimental tool, particularly in understanding the effects of additional electronic filtering on the dynamics to enable more robust measurement techniques.

However, for an intuitive understanding of the processes involved, and the possibility of fitting data to values of the optical rigidity K_0 , G_L , and G_f , we desire an analytically tractable model. A block diagram of the optically-coupled pendulums and control systems is shown in Figure 3-5. The electronic filters for the frequency

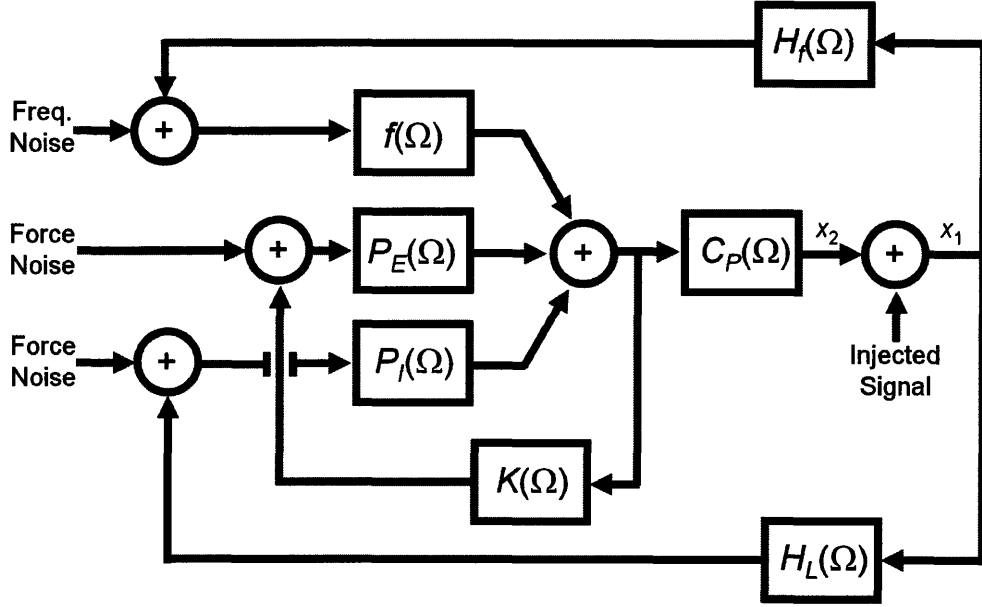


Figure 3-5: Block diagram for the optomechanical and control systems.

and length paths are $H_f(\Omega)$ and $H_L(\Omega)$, and are shown in Figure 3-2. The IM and EM transfer functions are given by $P_I(\Omega)$ and $P_E(\Omega)$, and differ in their values for Ω_p and Q . We assume the optical rigidity only acts on the end mirror, whose small mass dominates the dynamics. The VCO transfer function $f(\Omega)$ is assumed to be flat over the frequency range of interest. The cavity response has a frequency dependence due to the response time γ^{-1} ; the cavity transfer function $C_P(\Omega)$ is given by (3.1). The error signal x_2 plus the injected signal form the control signal x_1 which is sent via the two feedback paths to drive the system. Note that all length control is done on the IM; the EM is only damped by the OSEMs to try to pin its position and alignment.

A drive signal is injected and the transfer function x_2/x_1 is measured. By considering the length and frequency paths separately, we can solve for the total loop gain of the system $G_{\text{loop}}(\Omega)$ by superposition. By Black's formula, $G_{\text{loop}}(\Omega)$ is suppressed by the optical feedback loop with $P_E(\Omega)$ and $K_{\text{opt}}(\Omega)$. We then express the loop gain as

$$G_{\text{loop}}(\Omega) = \frac{[G_f H_f(\Omega) f(\Omega) + G_L H_L(\Omega) P_I(\Omega)] C_P(\Omega)}{1 - P_E(\Omega) K(\Omega)}. \quad (3.5)$$

In measuring the optical spring transfer function, we have four experimental controls. As was shown above, adjusting the gains G_L and G_f tunes the placement of Ω_c and Ω_b . We can adjust the intracavity power I_0 with the use of a volume-control half-wave plate and the detuning δ by applying a bias to the OSEMs. With these experimental controls, several orders of magnitude in K_0 can be explored experimentally.

Chapter 4

Results and Conclusions

We performed measurements of the optomechanical systems described in the previous chapter during the 2005-2006 academic year. Experiments on the P1 cavity lasted from September to December 2005, and measurements on the P2 cavity began in February 2006 and will continue into June 2006.

In this chapter we describe our measurements of the PI and OS and the subsequent analysis performed. In particular, we describe how the data were taken, the methods used to process it, and describe the significance of this work.

4.1 Parametric Instability

As many scientific discoveries often are, our observation of a parametric instability in the P1 cavity was accidental. During measurements of the loop gain $G_{\text{loop}}(\Omega)$ we found a spectral line at $\Omega_d = 2\pi \times 28.188$ kHz ring up. Within 10-20 seconds, the oscillations at Ω_d were large enough to drive the cavity out of lock.

Because the mechanical properties of the 250 g mirrors had already been studied, we knew that the oscillations at $\Omega = \Omega_d$ were occurring at the mirror drumhead mode frequency. In order to ensure the ringup was PI and not some feedback-induced instability, we employed several strategies. First, as expected for a PI, the mode only became excited on one side of the cavity resonance. Recall from Section 2.5 that the drumhead mode will only be unstable when the Stokes mode is built up at a faster

rate, which only occurs only for $\delta_\gamma > 0$. We also found, as one would expect, that the measured ringup time (τ' , defined as the time it takes for the amplitude to increase by a factor of e) varied with the detuning and input power. From our definition of the susceptibility Eq. (2.35), repeated here,

$$R \equiv \frac{K(\Omega_d)Q}{M^*\Omega_d^2}, \quad (4.1)$$

we note that R depends on the optical rigidity $K(\Omega)$, which increases with increasing power and detuning.

Also, to ensure that the ringup was not caused by a feedback effect, we explored the effects of varying the frequency path gain G_f . Importantly, we found that the mode could be stabilized as G_f was raised. To prove that the effect was not feedback related, we set G_f to zero and the mode remained unstable. Because the ringup occurred when the feedback gain was zero, the ringup is clearly not due to a feedback-related instability, and must in fact be a PI.

4.1.1 Variation with Cavity Detuning

To characterize the PI, we explored the dependence of the susceptibility R on detuning and power, and compared to our model and to a numerical solution of the equation of motion

$$-\Omega^2\tilde{x} = -\left[\Omega_d^2 + \frac{i\Omega\Omega_d}{Q} + \frac{K(\Omega)}{M^*}\right]\tilde{x} + \frac{\tilde{F}_a}{M^*}. \quad (4.2)$$

Because R is related to the Q' resulting from the optomechanical coupling, one expects to find the effect of varying R in the ringup time τ' of the mode. By substituting the expressions Eqns. (2.28) and (2.30) into Eq. (2.27) and investigating the limit $\Theta \ll \Omega_d$, we notice

$$Q' = \frac{Q}{1-R}. \quad (4.3)$$

We also know that Q' represents the number of oscillations in a ringdown (or ringup for an unstable mode). Because of the weakness of the optical rigidity, the resonant frequency shifts only a fraction of a Hz from Ω_d , and Q' and Q are simply linear

multiples of the modified and natural ringup times τ and τ' . Therefore, to determine R we simply relate the modified and natural ringing times as

$$R = 1 - \frac{\tau}{\tau'}. \quad (4.4)$$

To measure the ringup/ringdown times of the drumhead mode we use a standard lock-in technique. The error signal is fed to a lock-in amplifier, which acts as a narrow band-pass filter near Ω_d . This is done by first mixing the error signal with a demodulation sinusoid at Ω_{LI} , which is slightly offset from Ω_d . The resulting signal is then low-pass filtered to remove any other dynamical effects, leaving a ringup at the difference frequency $\Omega_{\text{diff}} = |\Omega_{LI} - \Omega_d|$. In order to ensure that the ringup times are not affected by the frequency control at Ω_d , we inserted a strong notch filter (-60 dB) centered at Ω_d into the frequency control path. The ringup times we observed varied between about 4 and 40 seconds.

To measure values $R > 1$ we simply detune the cavity from resonance and capture the ringup of the drumhead mode. The lock-in signal $v(t)$ is saved on floppy disk and fit to an exponentially growing sinusoid

$$v(t) = Ae^{t/\tau'} \sin(\Omega_{\text{diff}}t + \phi) + c. \quad (4.5)$$

An example fit can be seen in Figure 4-1, in which only a short portion of the ringup is displayed for clarity. The detuning is found by comparing the transmitted intensity $I_t = |E_t|^2$ observed during the lock-in measurement to the maximum intensity I_t found when the cavity is resonant. Because I_t and the stored power W are directly related, by rearranging Eq. (2.13),

$$\delta_\gamma = \sqrt{\frac{I_{t0}}{I_t} - 1} \quad (4.6)$$

where I_{t0} is the resonant transmitted power. We found that the transmitted power frequently fluctuated by about 3% of its value; this error source is propagated to contribute to error in the detuning.

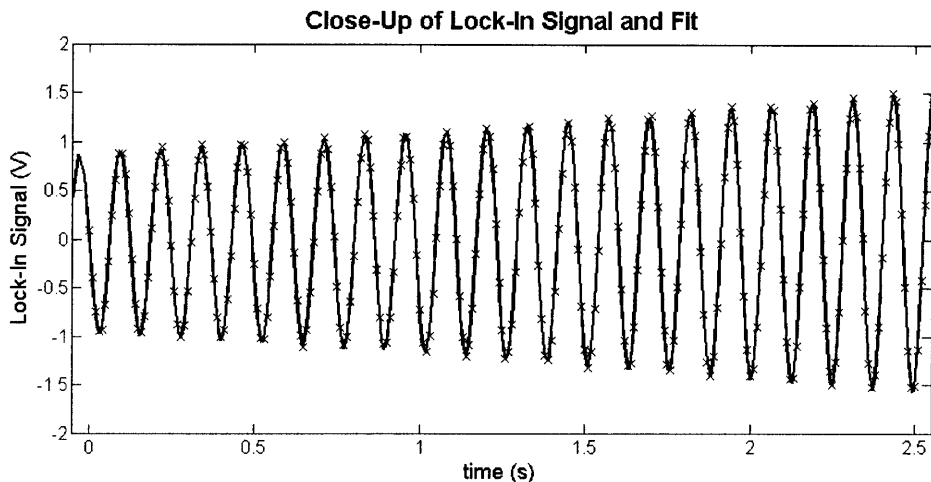


Figure 4-1: Zoom view of PI ringup data for $R > 1$. The \times 's are measured data points, and the dashed curve is a 5 parameter fit to Eq. (4.5).

To find the unmodified ring time we detuned the cavity to observe the ringup, and then quickly tuned the cavity back to resonance. The data consist of an exponentially damped sinusoid, whose characteristic decay time is τ . Averaging over several measurements made over a several hour period, the ring time was found to be $\tau = 8.3 \pm 0.8$ s.

Measuring values $R < 1$ was done in a similar way to τ . The mode was first excited by detuning to the unstable side of the resonance; we then quickly detuned to the cold-damping side of the resonance and captured the mode ringdown. In this way, we can construct the dependence of R on the detuning on either side of the resonance.

The measured values of R and their associated errors are plotted against the detuning in Figure 4-2. The horizontal errors are due to an inability to measure the transmitted power to more than about 5% accuracy, which propagates to error in the detuning. The vertical errors are due both to statistical error in fitting τ' to the time series and error in the Q of the drumhead mode. We found that, from measurement to measurement, values of Q (derived from measurements of τ) changed on the order of 20%. The solid curve in Figure 4-2 is found by numerically determining the poles of the optical rigidity $P_{OR}(\Omega)$ as a function of δ_γ .

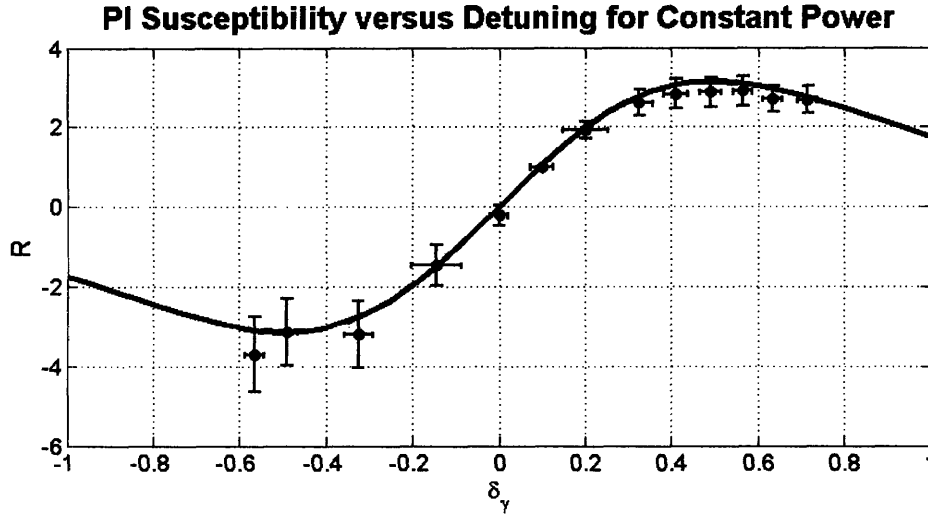


Figure 4-2: The PI Susceptibility is plotted against the normalized detuning δ_γ for constant input power. The solid curve is a theoretical prediction with no free parameters.

4.1.2 Determination of the Modal Mass

One parameter in the theoretical calculation of R as a function of δ_γ has not been discussed. The modal mass M^* of the drumhead motion needs to be determined experimentally. Although we have assumed that the resonant frequency Ω_d remained constant with the optical coupling, we can measure a small frequency shift in $\Omega_d \rightarrow \Omega'_d$ as we vary the detuning. We find the frequency shift between $\delta_\gamma = 0.715$ (the rightmost point in Figure 4-2) and $\delta_\gamma = 0$ by subtracting the Ω_{diff} 's calculated by the fitting process to be $\delta\Omega_d = 0.11 \pm 0.1$ Hz. Ω'_d is related to Ω_d by the optical rigidity as

$$\Omega_d'^2 = \Omega_d^2 + \frac{K(\Omega_d)}{M^*}, \quad (4.7)$$

and by rearranging this we find $M^* = 120 \pm 4$ g.¹ The errors on Ω_d are statistical and are due to the 95% confidence bounds on the fit of Eq. (4.5) to the time series.

The similarity of the values of M^* and μ , the reduced mass, is entirely coincidental.

¹In measuring the optical spring, we measure $K_0 \approx K(\Theta)$ by measuring the altered resonant frequency Θ and calculating $K = \Theta^2/\mu$. We compute $K(\Omega_d)$ according to the assumed frequency dependence, but find only a small shift as $\Omega_d < \gamma$, the breakpoint of $K(\Omega)$. This measurement is discussed in the following section on the OS.

A finite element analysis of the mirror predicted that M^* should be approximately 0.09 kg. Our larger value, however, is consistent with the fact that the laser beam might not be perfectly centered on the mirror. If the beam spot is shifted spatially on the mirror surface, the mechanical response of the drumhead mode will be reduced because the spot hits a less sensitive portion of the mirror. The effect of this is that for a given force, the amplitude of motion is reduced, thereby causing an apparent increase in mass.

4.1.3 Variation with Input Power

Above we discussed the effect of variable detuning on the instability while keeping the power fixed. Here we explore the effect of varying the power while keeping the detuning fixed. This is done experimentally by first rotating the volume control half-wave plate and observing the effect of the transmitted light. Once I_{40} is determined for a given input power, the cavity is detuned to the 75% power point, and the measurement of the ringup is captured.

The expected dependence of R on the incident power I_0 is linear; R depends directly on $K(\Omega)$, which varies directly with I_0 . Because we always detuned to the same position, we only needed to measure ringup times. The data are plotted in Figure 4-3, along with a numerical solution to the equation of motion. The horizontal errors are due again to a 3% uncertainty in power measurement, and the vertical errors are due to the 20% uncertainty in the Q .

The data clearly show a linear trend as the theory predicts. However, due to issues of our inability to very precisely calibrate the stored power to the detected transmitted intensity photodetector signal and the large variation of measured τ values, the solid curve is a two-parameter linear fit.

4.2 P1 Optical Spring

Our P1 cavity parameters were $T_1 = 0.64\%$ and $L = 1$ m, which yielded a linewidth $\gamma = 2\pi \times 75$ kHz, and a finesse of $\mathcal{F} = 1000$. As found in Section 2.3.1, the optical

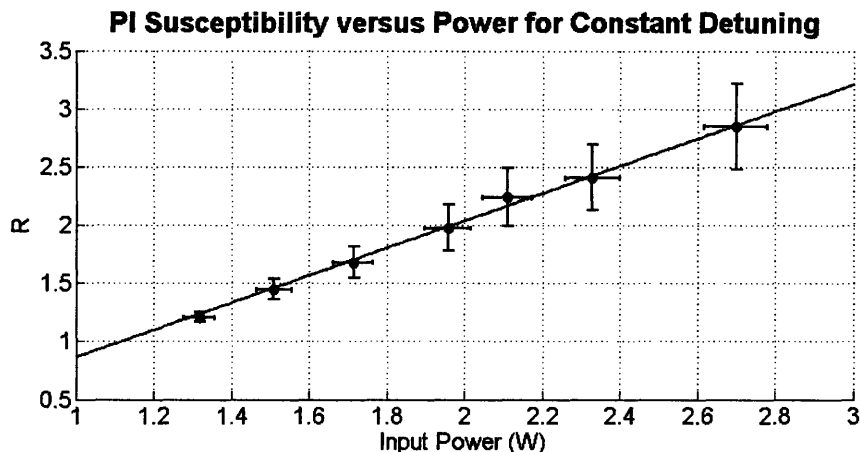


Figure 4-3: The PI Susceptibility is plotted against the input power for constant detuning. The solid curve is a two parameter fit, allowing for uncertainty in the scaling of the power and

rigidity K_0 is maximized when the cavity is detuned to the 75% power point, which corresponds to $\delta \approx 40$ kHz.

Without any alterations to the control system, the PI would drive the cavity out of lock while measuring the OS. In order to ensure that this would not happen, we suppress the PI by increasing G_f . The increase in G_f pushed Ω_b out to $2\pi \times 50$ kHz so the PI was well within the locking bandwidth of our control system. G_L was picked so that the crossover frequency Ω_c fell at $2\pi \times 300$ Hz. With this control configuration, a no PI was observed. This in itself is an important achievement, as it shows that the PI that threatens Advanced LIGO can be controlled by feedback.

To measure the effects of the optical spring, we sought to measure a displacement/force transfer function of the optically coupled pendulum. This was done by applying a swept-sine signal to the coil actuators of the OSEMs between $\Omega = 2\pi \times 10$ and $2\pi \times 200$ Hz. We then simply compare the driving force to its response in the PDH error signal to characterize the optical spring. The transfer function measurement takes several minutes because a large degree of averaging is needed to alleviate the effects of noise in the system.

The P1 OS data is shown in Figure 4-4. The measured data are the points, and

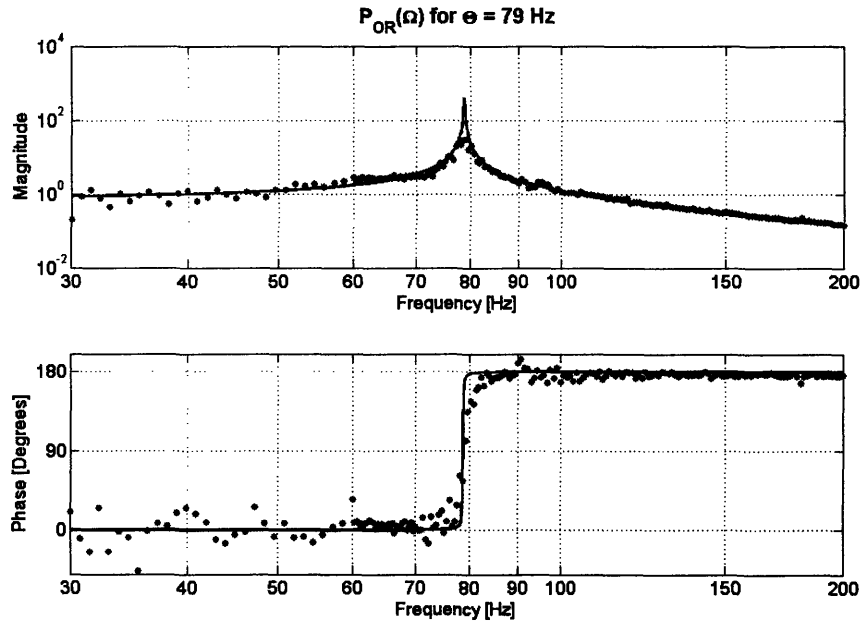


Figure 4-4: P1 OS transfer function $P_{OR}(\Omega)$ data (dots) and 1 parameter fit of Θ (solid), found to be $2\pi \times (79 \pm 1)$ Hz.

the solid curve is found as a one parameter fit (of Θ) to $P_{OR}(\Omega)$.² We find the shifted resonant frequency to be $\Theta = 79 \pm 1$ Hz, which yields an optical rigidity $K(\Theta) = (3.08 \pm 0.09) \times 10^4$ N/m. Because $\Theta \ll \gamma$, $K(\Theta) = K_0$, the rigidity at DC. Note that the optical coupling has produced an oscillator with a rigidity approximately 6000 times that of the uncoupled pendulum. At the time of the measurement in November 2005, this optical rigidity was unprecedented, and has since only been surpassed by our Phase 2 measurement.

One striking feature of the data in Figure 4-4 is the fact that the phase *increases* by 180° at the resonance. The phase damped harmonic oscillator, due to its positive Q value, typically decreases by 180° at its resonant frequency; clearly here our altered Q' is negative, corresponding to an anti-damping term in the equation of motion. The unstable nature of an optical spring had long been predicted, but this measurement is the first to demonstrate the physical effects of an anti-damping term. Due to

²The unmodified Q of the pendulum mode was known to be approximately 10^5 , which, along with Θ , specifies the modified Q' of the optical spring.

the strength of the length control system at frequencies less than Ω_c , however, the instability was successfully stabilized by feedback. This also marks an important step for the use of optically enhanced rigidities in quantum non-demolition interferometers, and devices designed to create non-classical states of light by ponderomotive effects [19].

The data is plotted without error bars as the driving signal to response signal coherence was typically very close to unity. The measurement only lost coherence very close to the resonance peak. The reason we expect we were unable to resolve the peak of the resonance is due to power fluctuations in the cavity. We noticed a parasitic RF amplitude modulation of the incident light, most likely due to some polarization mismatching in the stabilization and mode-cleaning stages of the light preparation. This caused shifts in power entering which varied on the order of seconds, resulting in an inability to resolve the shape of the resonant peak.

4.3 P2 Optical Spring

The coupled oscillator used in Phase 2 added a significant amount of complexity to the experiment. In P2 we used an input mirror with nearly an order of magnitude lower transmission $T_1 = 0.08\%$. This resulted in a higher finesse of $\mathcal{F} = 8000$ and higher stored power, with lower linewidth $\gamma = 2\pi \times 10$ kHz. In this section we describe the loop gain measurements and characterization of the stronger optical spring. We also describe and quantify the noise suppression due to the optical rigidity, and place the results within a context of laser cooling and attempts to create macroscopic quantum superpositions.

We note that PI was not observed during P2. This is due to the fact that the mechanical Q of the P2 IM was observed to be roughly 100 times smaller than that for the P1 IM.

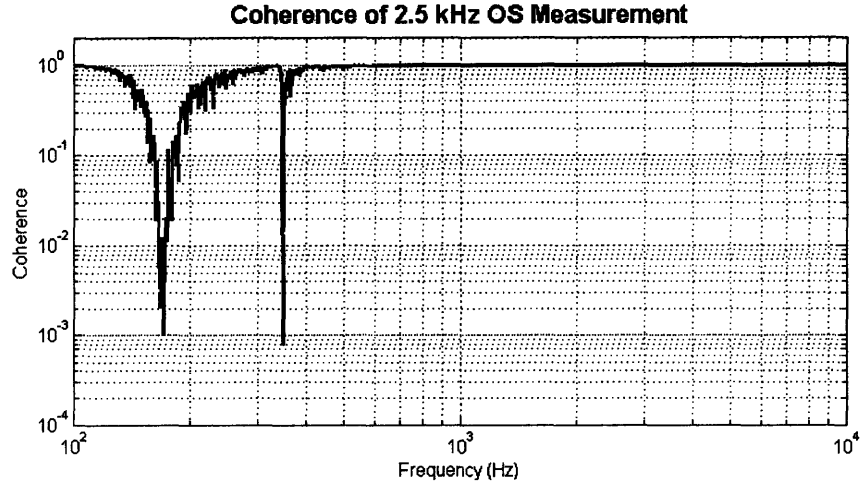


Figure 4-5: Coherence of $G_{\text{loop}}(\Omega)$ measurement for the $\Theta \approx 2.5$ kHz OS measurement. The coherence is unity except at the longitudinal resonance near 170 Hz and the pitch resonance near 350 Hz.

4.3.1 Loop Gain Measurement

We seek to measure and characterize optical springs at much higher frequency. Because of the higher finesse and lower mass of the EM, we can experimentally explore a very different regime of optical rigidity, in which the altered resonance Θ is in the same order of magnitude as the cavity linewidth.

Because Ω_c is typically a few hundred Hz, we cannot simply push directly on the mirrors and observe the effect in the error signal. We add a driving signal to the error signal which forms a control signal sent in parallel along the length and frequency paths (“Injected Signal” in the schematic of Figure 3-5). Because the EM has a mass of 1 g compared to the 250 g IM, optomechanical effects play a much greater role on the dynamics of the EM and the reduced mass $\mu \approx 1$ g.

The loop gain $G_{\text{loop}}(\Omega)$, as given by Eqn. (3.5) was measured for several input powers and detunings. The measurements were taken on a spectrum analyzer, which produced a swept-sine driving signal between 100 Hz and 10 kHz. With significant signal averaging, all data had unity coherence except near the 170 Hz longitudinal mode of the EM where the coherence frequently dropped to below 10^{-2} . For an example coherence plot, see Figure 4-5.

4.3.2 Optical Spring Characterization

To find the optical spring transfer function, we use the following technique. After measuring $G_{\text{loop}}(\Omega)$, we perform a 6 parameter fit ($K_0, G_L, G_f, Q, \Omega_p, \bar{\delta}_\gamma$) to Eq. (3.5). From this fit, we then compute the loopgain of an equivalent system without optical rigidity: we define and compute $G_{\text{loop}}^0(\Omega) \equiv G_{\text{loop}}(\Omega)|_{K_0=0}$. Dividing $G_{\text{loop}}(\Omega)$ by $G_{\text{loop}}^0(\Omega)$ gives, according to Eq. (3.5),

$$\frac{G_{\text{loop}}(\Omega)}{G_{\text{loop}}^0(\Omega)} = \frac{1}{1 - K(\Omega)P_E(\Omega)}. \quad (4.8)$$

From Eq. (2.27) we expect $P_{OR}(\Omega)$ to have the form

$$P_{OR}(\Omega) = \frac{P_E(\Omega)}{1 - K(\Omega)P_E(\Omega)}, \quad (4.9)$$

so clearly we can determine P_{OR} experimentally by calculating

$$P_{OR}(\Omega) = \left(\frac{G_{\text{loop}}(\Omega)}{G_{\text{loop}}^0(\Omega)} \right) P_E(\Omega). \quad (4.10)$$

We, however, did not directly measure $P_E(\Omega)$ or $G_{\text{loop}}^0(\Omega)$, although this would have been possible. $G_{\text{loop}}^0(\Omega)$ can be found by measuring the loop gain at 0 detuning, but due to experimental imprecision, it is difficult to place the cavity exactly on resonance, leaving some parasitic optical rigidity. $P_E(\Omega)$ can be measured with extremely low power, however, as the input power is lowered it becomes increasingly difficult to lock the cavity.

OS data and fits, along with the (theoretical) unmodified EM transfer function $P_E(\Omega)$ are plotted in Figure 4-6. The four transfer functions plotted span roughly an order of magnitude in Θ , and the K_0 values range from $(1.18 \pm .01) \times 10^4$ to $(9.60 \pm 0.12) \times 10^5$ N/m. Length gains G_L were all between 10^{10} and 10^{11} , and G_f lay between 10^6 and 10^7 .

The fitting was done with a custom nonlinear fitting routine in MATLAB by using Newton's method to search for minima of the χ^2 in parameter space. The pitch mode

near 350 Hz was not modelled, and data between $f = 220$ and $f = 500$ Hz was not included in the fit. In addition, two other narrow features can be observed, near $f = 1.3$ kHz and $f = 3$ kHz. We expect that these spectral features are harmonics of the fundamental violin mode of the suspension cable at $f \approx 670$ Hz. A plot of the normalized residual

$$E(\Omega) = \frac{|G_{\text{loop}}^f(\Omega)| - |G_{\text{loop}}(\Omega)|}{|G_{\text{loop}}(\Omega)|}, \quad (4.11)$$

where $G_{\text{loop}}^f(\Omega)$ is the calculated fit, for the 5 kHz OS is shown in Figure 4-7. As this plot subtracts the predicted signal from the data, it is essentially a plot of the random fluctuations in the data and the unmodeled modes. Away from either the pitch mode or the violin modes, we find that the noise stays very near zero, and has fluctuations of about 10% of its value. We then take this as the statistical error on the data, and calculate the χ_ν^2 values for all the fits. We find values between 0.8 and 2.2 for all fits except for the 950 Hz OS, which had $\chi_\nu^2 = 6.32$. As can be seen in Figure 4-6) this measurement had substantial noise at low frequencies, most likely due to significant power fluctuations on the time scale of several seconds.

We notice two important effects in Figure 4-6 as the optical rigidity increases. First, the optical springs still have anti-damping as discussed above, as we see again that the phase increases 180° at the resonance. The unstable nature was also noticed in practice, as when the control system gains were lowered too far, the optical spring drove the cavity out of lock. Second, as Θ moves to higher frequencies, the linewidths of the optomechanical resonance peaks broaden. The effect can also be seen in the phase plots, as the rise near resonance becomes more gradual as Θ increases. This is a direct consequence of the unified feedback model of optical rigidity, as discussed in Chapter 2.

One spurious effect we noticed is that with higher input power, the EM resonant frequency Ω_p and corresponding Q were modulated. Specifically, as the intracavity power increased, Ω_p increased (to about $2\pi \times 175$ Hz) and Q decreased (to about 65). We hypothesize that this is a thermal effect due to the high circulating powers present for the 5 kHz OS. As the power increases, the laser beam heats the mirror.

This results in heat flow along the glass fibers to the “reservoir” steel shell. As a result of the heating of the fibers, they become more bowed, and thus the resonance increases. The increased thermal noise due to the higher temperature might explain the decrease in Q as well.

4.3.3 Noise Suppression

Another striking feature of the OS data in Figure 4-6 is the reduction of the low frequency response of $P_{OR}(\Omega)$ as Θ increases. This is exactly the noise suppression effect discussed in Chapter 2. It is very easily understood; as the spring becomes stiffer, for a constant force the resulting displacement is much smaller.

To quantify the noise suppression generated by the optical rigidity, we plot the ratio of responses $x/x^{(0)}$ of the optically stiffened pendulum to the EM response $P_E(\Omega)$. According to Eq. (2.34), we expect the noise suppression to have the form

$$\left| \frac{x}{x^{(0)}} \right| = \frac{\Omega^2}{\Theta^2 - \Omega^2}. \quad (4.12)$$

In Figure 4-8, we plot the ratio of the responses $|x/x^{(0)}|$ evaluated at $\Omega = 2\pi \times 100$ Hz, and find that the noise suppression we observe is consistent with the theory. The resonant frequencies Θ are determined by finding the frequency at which the phase has climbed to 90° , and the error bars reflect the frequency width at which $|\angle P_{OR}(\Omega) - 90^\circ| < 10^\circ$. The vertical error bars are due to noise in the response near 100 Hz, and reflect the standard deviation of the response within 10 Hz of 100 Hz. The solid curve is a plot of Eq. (4.12) evaluated at $\Omega = 2\pi \times 100$ Hz.

4.4 Towards the Quantum Limit

Although the EM would certainly not be cool to the touch, it is interesting to consider the increased rigidity as effectively cooling the mirror. This presents an alternate “laser cooling” scheme to the optical molasses effect or Zeeman slowing used in atomic physics. Here, the cooling of the mirror is done by increasing the strength of its

harmonic trap via radiation pressure [24]. If we can define an effective temperature T_{eff} of the mirror, it is an interesting question to ask whether, as the rigidity increases, $k_B T_{\text{eff}}$ approaches $\hbar\Theta$, the point at which the oscillator will begin to exhibit its quantum mechanical nature.

Metzger and Karrai [14] show that if the limiting noise source in an optomechanical system is thermal noise, given by

$$\langle z_{\Omega}^2 \rangle = \frac{4k_B T}{K_m} \frac{\Omega_0 \Gamma_0}{(\Theta^2 - \Omega^2)^2 + (\Gamma_{\Theta} \Omega)^2} \frac{\delta\Omega}{2\pi} \quad (4.13)$$

where $\langle z_{\Omega}^2 \rangle$ is the mean squared displacement within $\delta\Omega$ of Ω , K_m is the natural spring constant, Ω_0 is the natural frequency, Θ is the resonant frequency of the optically coupled system, Γ_0 is the damping rate Ω_0/Q , and $\Gamma_{\Theta} = \Theta/Q'$ is the modified damping. In our experimental regime $\Theta \gg \Omega_0$, we can integrate Eq. (4.13) over all Ω to find

$$T_{\text{eff}} = \frac{\Omega_0 \Gamma_0}{\Theta \Gamma_{\Theta}} T. \quad (4.14)$$

To put it concretely, if we begin with an oscillator with $\Omega_0 = 2\pi \times 171$ Hz and assume a realistic Q of 10^4 ,³ $\Gamma_0 = 10^{-4}\Omega_0$. The optically stiffened values are $\Theta = 2\pi \times 5$ kHz, and as a first guess we take $\Gamma_{\Theta} \approx \Theta$ as evidenced by the extremely broad resonance feature in Figure 4-6. Assuming room temperature T , this gives $T_{\text{eff}} \approx 3.5 \times 10^{-7}$ K. To estimate the temperature needed to approach the quantum limit, we set $k_B T_{\text{eff}} = \hbar\Theta$ and find $T_{\text{eff}} = 2.4 \times 10^{-7}$, which would indicate that our system is within an order of magnitude of the quantum limit for a 1 g object. Moreover, if the 171 Hz resonance is replaced with a 1 Hz resonance as is planned for a particular experiment, it may be possible to reach $T_{\text{eff}} \approx 10^{-10}$ K.

However, we have neglected some technical issues. We have assumed that thermal noise in the suspension is the dominant noise source, but it has been shown that at these frequencies it is the mirror coating thermal noise that enters most prominently. In addition, with $\Theta \gg \Omega_0$, as we have shown, strong optical anti-damping occurs, and severe instability will ensue unless the mode is stabilized through an external control

³With some present materials it is possible to attain a mechanical Q of more than 10^6 .

system. However, in this manner, we can effectively control the optical damping Γ_{Θ} .

In our system, the dominant noise in the bandwidth of interest is frequency noise. To calculate T_{eff} for the optical spring mode, we solve

$$\frac{1}{2}K_0\langle\tilde{x}\rangle^2 = k_B T_{\text{eff}}, \quad (4.15)$$

where $\langle\tilde{x}\rangle$ is the RMS residual motion in the OS mode, for T_{eff} . Once the error signal is measured, $\langle\tilde{x}\rangle$ can be found by integrating the noise spectrum over the linewidth of the mode. A few technical issues have prevented us from acquiring data that will give a good representation of $\langle\tilde{x}\rangle$, as the dominant motion in the system is that created by our servo system to maintain cavity lock and to prevent a runaway instability of the OS, rather than motion due to laser frequency or phase fluctuations. To measure a proper spectrum, we need to lower the control system gains such that residual thermal motion becomes the dominant effect. Achieving this experimentally has been a challenge, but we are hopeful to gain information about the cooling effects soon.

Our current experiment is many orders of magnitude away from the our predicted lower limit with this particular mechanical system. To be able to observe a quantum state for this system, we need to improve several noise sources for the system. The primary concern is to reduce laser noise, both frequency and intensity; proposals exist to use an interferometer configuration in which the oscillator degree of freedom is the differential arm motion, which allows for common mode cancellation of the laser noise [19]. The scheme was originally proposed to measure non-classical states of light produced by ponderomotive coupling, but it may be possible to use the configuration to attempt QND measurements of the quantum state of a 1 g mass.

4.5 Concluding Remarks

We have developed a model describing the modified dynamics of the suspended mirrors of a Fabry-Perot cavity when coupled to an intense laser beam. We described

two important radiation pressure effects that one expects in a Fabry-Perot cavity, the OS and the PI. In the OS, the optical rigidity $K_0 \gg \Omega_p^2/\mu$, such that the resonant frequency of the oscillator can be altered significantly. During P2, we measure an optical rigidity as strong as $(9.60 \pm 0.12) \times 10^5$ N/m; this corresponds roughly to the same stiffness as if the optical beam were replaced by a diamond rod of the same dimensions. We demonstrate the unstable nature of the OS by observing a phase increase at the resonance, and by observing an instability that drove the cavity out of lock when the control system gains were reduced. We also illustrate an impressive suppression of force noise by the optical rigidity. For $\Theta = 2\pi \times 5$ kHz, we observe a noise suppression of nearly 1000 at 100 Hz over a simple oscillator.

In the PI, although the optical rigidity is much weaker than the mechanical rigidity, the equation of motion introduces an anti-damping term for some values of the detuning such that an instability develops and a mechanical mode can be pumped hard enough to drive the cavity out of lock.

The effects we describe are an important classical stepping stone leading to a lake of quantum mystery. It was understood even during the dawn of quantum mechanics that the theory set no size restriction on a wave function. So-called ‘‘Schrödinger Cat’’ states have been produced and measured that consist of coherent superpositions of approximately 10^{14} atoms. In this work, we lay the groundwork for preparing a mirror weighing 1 g in a quantum state by coupling it to an intense optical field and creating an enhanced rigidity. As we discussed above, there are certainly several more technical noise sources to take care of before we reach a quantum regime, but an experimental design exists and is currently in construction to achieve this task [19].

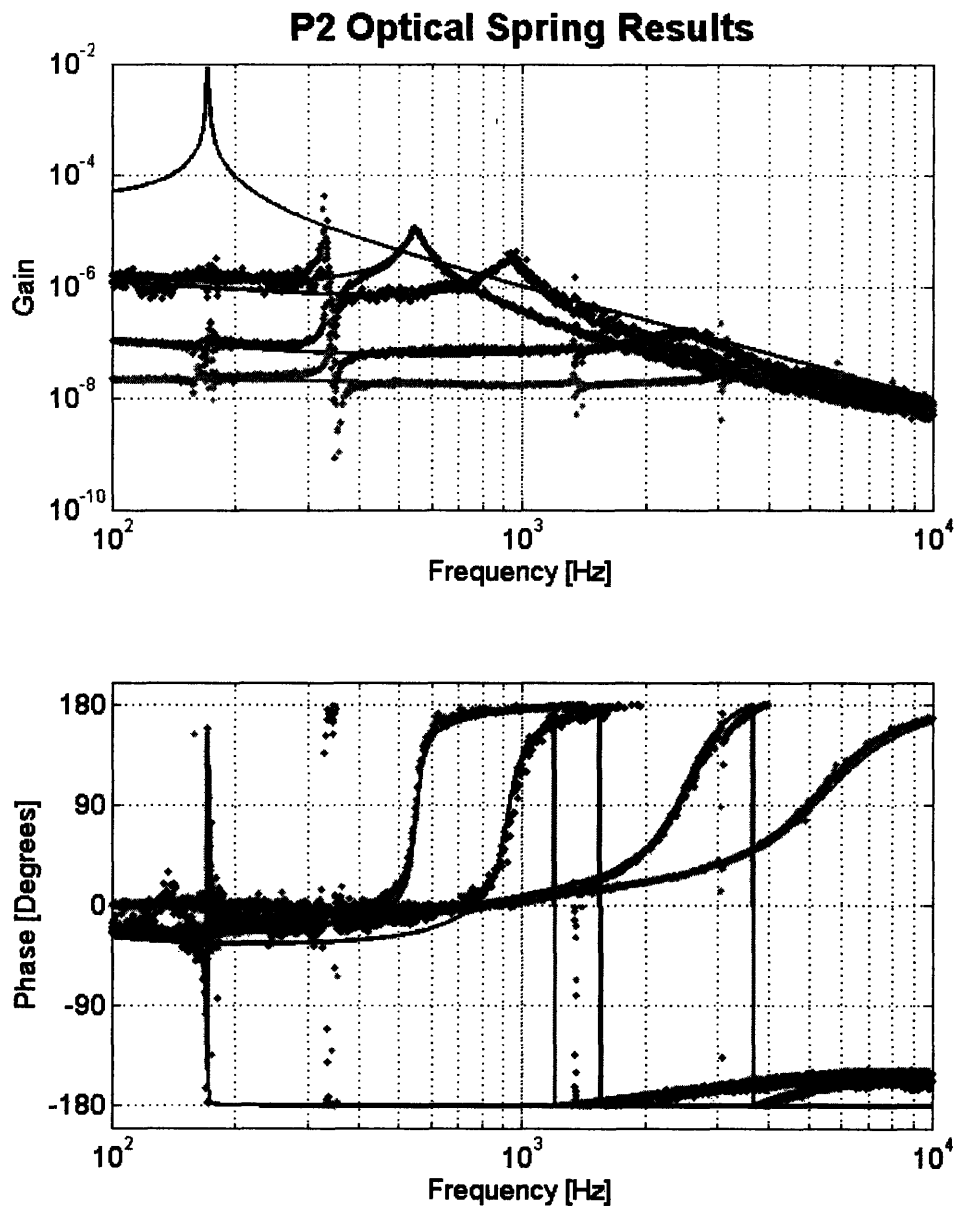


Figure 4-6: OS transfer functions $P_{OR}(\Omega)$ calculated from loop gain data and fit parameters according to Eq. (4.10) for four values of Θ between $2\pi \times 550$ Hz and $2\pi \times 5$ kHz. The solid black curve is the unmodified end mirror response $P_E(\Omega)$, and along with each dataset is its corresponding fit.

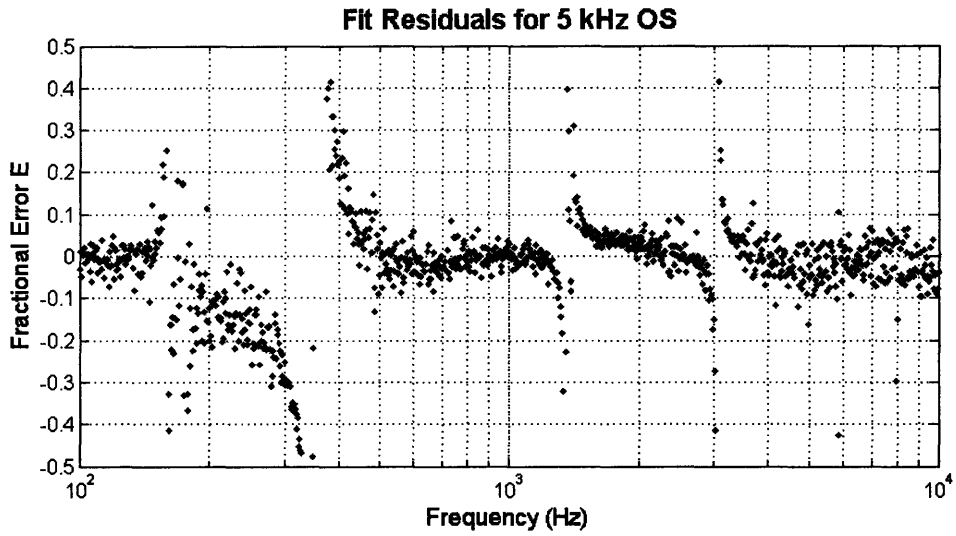


Figure 4-7: Plot of normalized residual $E(\Omega)$, defined in Eq. (4.11), for the 5 kHz OS.

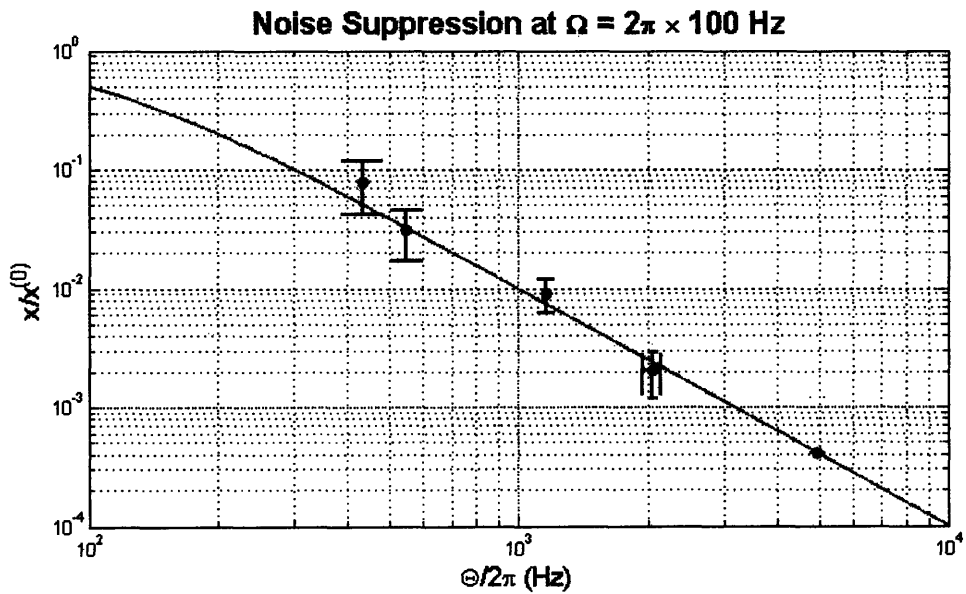


Figure 4-8: Illustration of noise suppression: ratio of optically stiffened pendulum response to EM response at $\Omega = 2\pi \times 100$ Hz as a function of Θ .

Bibliography

- [1] E. Schrödinger, *Naturwissenschaften* **23**, 807 (1935).
- [2] C. Monroe, D. M. Meekhof, B. E. King, and D. J. Wineland, “A ‘Schrödinger Cat’ Superposition State of an Atom”, *Science* **272**, 1131 (1996).
- [3] W. Marshall, C. Simon, R. Penrose, and D. Bouwmeester, “Towards Quantum Superpositions of a Mirror”, *Phys. Rev. Lett* **91**, 130401 (2003).
- [4] S. Bose, K. Jacobs, and P. L. Knight, “Scheme to Probe the Decoherence of a Macroscopic Object”, *Phys. Rev A* **59**, 3204 (1999).
- [5] A. D. Armour, M. P. Blencowe, and K. C. Schwab, “Entanglement and Decoherence of a Micromechanical Resonator via Coupling to a Cooper-Pair Box”, *Phys. Rev. Lett.* **88**, 148301 (2002).
- [6] J. R. Friedman, V. Patel, W. Chen, S. K. Tolpygo, and J. E. Lukens “Quantum Superposition of Distinct Macroscopic States”, *Nature (London)* **406**, 43 (2000).
- [7] M. Arndt, O. Nairz, J. Vos-Andreae, C. Keller, G. V. D. Zouw, and A. Zeilinger, “Wave-particle Duality of C_{60} Molecules”, *Nature (London)* **401**, 680 (1999).
- [8] T. Corbitt, J. Pelc, D. Ottaway, E. Innerhofer, D. Sigg, and N. Mavalvala, “Cavity Cooling of Gram-scale Mirrors as a Path to Quantum Effects on Macroscopic Oscillators”, in preparation.
- [9] T. Corbitt, D. Ottaway, E. Innerhofer, J. Pelc, and N. Mavalvala, “Measurement of Radiation-Pressure-Induced Optomechanical Dynamics in a Suspended Fabry-Perot Cavity”, submitted to *Phys. Rev. Lett.*

- [10] B. S. Sheard, M. B. Gray, C. M. Mow-Lowry, D. E. McClelland and S. E. Whitcomb, “Observation and Characterization of an Optical Spring”, *Phys. Rev. A*, **69**, 051801 (2004).
- [11] V. B. Braginsky, A. B. Manukin, and M. Yu. Tikhonov, *Sov. Phys. JETP* **31**, 829 (1970) *In Russian*.
- [12] A. Buonanno and Y. Chen, “Signal Recycled Laser-Interferometer Gravitational-Wave Detectors as Optical Springs”, *Phys. Rev. D* **65**, 042001 (2002).
- [13] T. J. Kippenberg, H. Rokhsari, T. Carmon, A. Scherer and K. J. Vahala, “Analysis of Radiation-Pressure Induced Mechanical Oscillation of an Optical Microcavity”, *Phys. Rev. Lett.* **95**, 033901 (2005).
- [14] C. H. Metzger and K. Karrai, “Cavity Cooling of a Microlever”, *Nature* **432**, 1002 (2004).
- [15] V. B. Braginsky, S. E. Strigin, and S. P. Vyatchanin, “Parametric Oscillatory Instability in Fabry-Perot Interferometer”, *Phys. Lett. A* **287**, 331 (2001).
- [16] W. Kells and E. d’Ambrosio, “Considerations on Parametric Instability in Fabry-Perot Interferometer”, *Phys. Lett. A* **299**, 326 (2002).
- [17] V. B. Braginsky, S. E. Strigin, and S. P. Vyatchanin, “Analysis of Parametric Oscillatory Instability in Power Recycled LIGO Interferometer”, *Phys. Lett. A* **305**, 111 (2002).
- [18] C. Zhao, L. Ju, J. Degallaix, S. Gras, and D. G. Blair, “Parametric Instabilities and Their Control in Advanced Interferometer Gravitational-Wave Detectors”, *Phys. Rev. Lett.* **94**, 121102 (2005).
- [19] T. Corbitt, Y. Chen, F. Khalili, D. Ottaway, S. Vyatchanin, S. Whitcomb and N. Mavalvala, “A Squeezed State Source Using Radiation-Pressure-Induced Rigidity”, *Phys. Rev. A* **73**, 023801 (2006).
- [20] P. Fritschel, *Gravitational Wave Detection, Proc. SPIE* **4856-39**, 282 (2002).

- [21] T. T. Lyons, *An Optically Recombined Laser Interferometer for Gravitational Wave Detection*, Doctoral Thesis, California Institute of Technology (1997).
- [22] D. J. Griffiths, *Introduction to Electrodynamics*, Third Edition, Prentice Hall.
- [23] V. B. Braginsky and S. P. Vyatchanin, “Low Quantum Noise Tranquilizer for Fabry-Perot Interferometer”, *Phys. Lett. A* **293**, 228 (2002).
- [24] P. F. Cohadon, A. Heidmann, and M. Pinard, “Cooling of a Mirror by Radiation Pressure”, *Phys. Rev. Lett.* **83**, 3174 (1999).